Title

LOW TEMPERATURE STUDIES: I. HEW ANTIFERROMAGNETIC RESONANCE EFFECTS IN THE IRON-GROUP FLUORIDES. II. IMPEDANCE MATCHING A JOSEPHSON-EFFECT GALVANOMETER BY MEANS OF A SUPERCONDUCTING TRANSFORMER

Author

Tennant, William Emerson.

Publication Date

1974-05-01

LBL-1844
c.1

LOW TEMPERATURE STUDIES:
I. NEW ANTIFERROMAGNETIC RESONANCE EFFECTS IN THE IRON-GROUP FLUORIDES
II. IMPEDANCE MATCHING A JOSEPHSON-EFFECT GALVANOMETER BY MEANS OF A SUPERCONDUCTING TRANSFORMER

William Emerson Tennant

(Ph. D. Thesis)

May 1974

Prepared for the U. S. Atpmic Energy Commission
under Contract W-7405-ENG-48

LOW TEMPERATURE STUDIES: I. NEW ANTIFERROMAGNETIC RESONANCE EFFECTS IN THE IRON-GROUP FLUORIDES

II. IMPEDANCE MATCHING A JOSEPHSON-EFFECT GALVANOMETER BY MEANS OF A SUPERCONDUCTING TRANSFORMER

Contents

LOW TEMPERATURE STUDIES: I. NEW ANTIFERROMAGNETIC RESONANCE EFFECTS IN THE IRON-GROUP FLUORIDES

II. IMPEDANCE MATCHING A JOSEPHSON-EFFECT GALVANOMETER BY MEANS OF A SUPERCONDUCTING TRANSFORMER

William Emerson Tennant

Lawrence Berkeley Laboratory
University of California
Berkeley, California

ABSTRACT

Far-infrared spectroscopy has revealed several new antiferromagnetic resonance effects in the iron group fluorides. In MnF_2 powders two previously unobserved magnetic absorptions have been seen at 7.7 cm^{-1} and 8.3 cm^{-1} just below the antiferromagnetic resonance at 8.7 cm^{-1}. The 8.3 cm^{-1} mode intensity increases as surface area increases, and may be tentatively identified as a surface magnon. The resonance intensity of this mode is 200 times stronger than a simple theoretical calculation for a surface magnon predicts.

Alloy systems of $(Co,Mn)F_2$, $(Fe,Mn)F_2$, and $(Zn,Mn)F_2$ have been studied throughout the concentration range. The magnetic-magnetic systems show two antiferromagnetic resonances, one associated with each magnetic ion. In CoF_2 with a small amount of Mn these modes are found at 28.5 cm^{-1} and 37 cm^{-1}, and in FeF_2: Mn at 50 cm^{-1} and 53 cm^{-1}. Two additional resonances have been observed in CoF_2 doped with 0.% - 10% Mn. These resonances (at 32 cm^{-1} and 35.5 cm^{-1}) are attributed to interactions between neighboring pairs and triplets of Mn ions in the CoF_2 host lattice.

Both the $(Co,Mn)F_2$ and $(Zn,Mn)F_2$ AFMR results show good agreement with the coherent potential approximation theory of these systems.

A superconducting transformer has been developed which increased the Johnson-noise limited range of a superconducting galvanometer by five orders of magnitude in resistance. A theory has been developed to evaluate the performance of superconducting galvanometer-transformer combinations. The working model transformer was found to perform according to the theory.

CHAPTER I. BACKGROUND FOR ANTIFERROMAGNETIC RESONANCE STUDIES

A. Characterization of Materials

The iron-group fluorides are one of the most extensively studied groups of antiferromagnets. The earliest antiferromagnetic resonance (AFMR) studies were by Johnson and Nethercott (using microwave techniques in MnF_2, 1959),[1] Ohlman and Tinkham (using far-IR spectroscopy in FeF_2, 1961),[2] and Richards (using far-IR spectroscopy in CoF_2 and NiF_2, 1963).[3,4] Since these initial investigations, much more research has been done by means of microwave, far-IR, Raman, and neutron diffraction techniques.[5-22] Nevertheless, because the antiferromagnetic resonances of these materials occur in a region of the spectrum which is not easily accessible by spectroscopic techniques, optical experiments are somewhat difficult and still reveal new effects even after fifteen years of research in this area. Before considering the present results, we shall summarize the properties of the materials being examined.

1. The Iron Group Fluorides MnF_2, CoF_2, FeF_2, ZnF_2

The crystal structure of the iron group fluorides is the tetragonal rutile structure shown in Fig. 1. This is a "squashed" BCC structure, and the eight corner sites are occupied by the next nearest neighbors (NNN) of the body center site. In the magnetic members of this group of materials, these corner sites are strongly coupled to the center sites by an antiferromagnetic superexchange interaction.[22,23] The nearest neighbor ions are separated by a lattice constant in the vertical (z) direction. In the magnetic materials the nearest neighbor exchange interaction is usually ferromagnetic.[22] Below the Neél temperature the spins are aligned parallel to the z (or c axis). The molten forms of these materials are miscible, and solutions crystallize as substitutionary alloys with the same rutile structure as the pure materials.[22] Table I lists some of the important properties of each compound.

TABLE I

Property	MnF_2	CoF_2	FeF_2	ZnF_2
Neél Temperature	67K [10]	37.7K [4]	78.35K [2]	N/A
AFMR (cm^{-1})	8.71±0.05 [1]	36.3 [4,13]	52.7±0.2 [2]	N/A
Linewidth (cm^{-1})	4.8×10^{-4} [10]	1.35 cm^{-1} [4]	≈ 1 cm^{-1} [2]	N/A
g-Factor	2.00 [1]	2.8,[4] 2.4 [12]	2.25±0.05 [2]	N/A
Exchange Integrals (cm^{-1}) [22]				
I_{NN}	0.440±0.003	-2.0±0.03 [31]	-0.05±0.003	N/A
I_{NNN}	2.48±0.003	12.3±0.03 [31]	3.64±0.003	N/A
$I_{3^{rd}NN}$	0.06±0.0003		0.19±0.003	N/A
Anisotropy Energy (E_A in cm^{-1})[22]	0.74±0.003	12.5±0.03	20.1±0.03	N/A
Effective Spin (S)[22]	2.5	0.5 [31]	2.0	N/A
Susceptibility (χ_1)	2.55×10^{-4}emu/gm [24]	6.00×10^{-4}emu/gm [25]		N/A
Sublattice Magnetization (M_s)	600 Oe [9]			N/A
Dielectric Const.			≈ 7 [26]	
Color [27]	Pink	Dark red	Brown	Clear
Specific Gravity [28]	3.98	4.46	4.09	4.95
Molecular Weight [28]	92.93	96.93	93.84	103.37
Lattice Parameters				
a,b	4.8734 Å [29]		4.6966 Å [2]	
c	3.3103 Å [29]		3.3091 Å [2]	

TABLE I (Cont.)

Property	MnF_2	CoF_2	FeF_2	ZnF_2
Solubility in H_2O [28]	0.48^{100} g/100 cc	Hot water	Slightly soluble	Hot water
Melting Point [28]	856 C	1200 C	> 1000 C	872 C
Cleavage Planes [30]	(110),(011)			

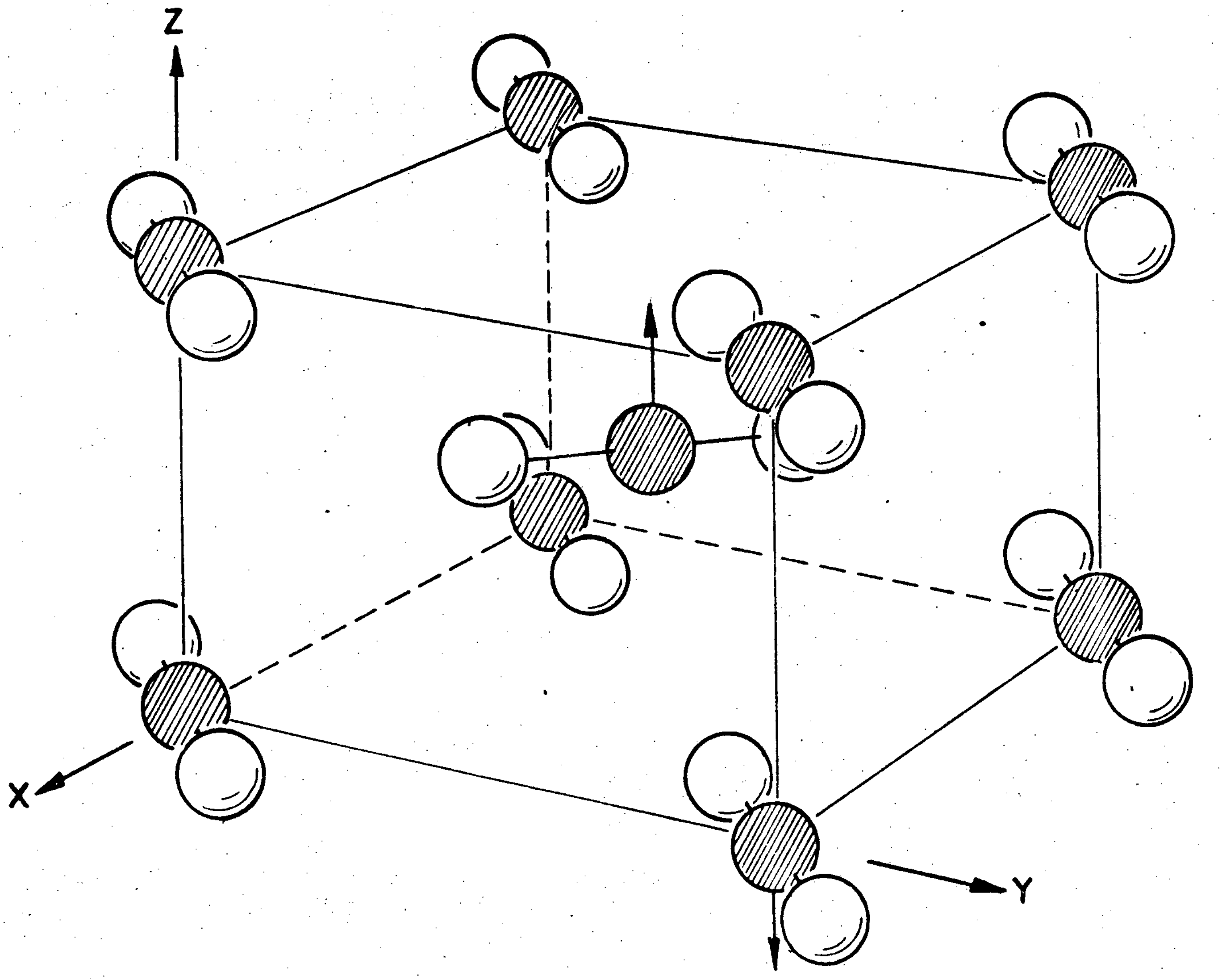

XBL738-1615

Fig. 1. Rutile crystal structure of the iron group fluorides. Dark spheres are metallic ions; lighter spheres are fluorine. Corner site spins are antiferromagnetically aligned with the center site spins, as shown by arrows.

B. Theoretical Introduction

1. Heisenberg Model - AFMR Derivation

The uniaxial antiferromagnets may be described by either a quantum mechanical or a classical approach, and sometimes even a mixture of the two is useful. We shall derive the antiferromagnetic resonance frequency by means of an essentially quantum approach and then show the transition to the linear chain approximation and to the classical molecular field approximation.

The Hamiltonian for the pure crystal of an iron group fluoride is[22]

$$\mathcal{H} = -\sum_i E_{A_i} S_z(i) P_i + \frac{1}{2}\sum_{ij} \vec{\vec{I}}(ij)\, \vec{S}(i) \cdot \vec{S}(j). \tag{1}$$

In this expression E_{A_i} represents the anisotropy energy of the i^{th} ion, $P_i = +1$ for spin up sites and -1 for spin down sites, and $\vec{\vec{I}}(i,j)$ represents the diagonal superexchange energy tensor. Our only concession to simplicity is the usual one made by replacing the true anisotropy expression by the above expression which is valid in the small spin deflection limit. We shall consider spin waves in the ladder operators $\overset{+}{S}(i)$ and $\overset{+}{S}(j)$. Re-writing the Hamiltonian in terms of these operators and S_z we have

$$\mathcal{H} = -\sum_i E_{A_i} S_z(i) P_i + \frac{1}{2}\sum_{ij} I(ij)\, S_z(i)\, S_z(j) + + \frac{1}{4}\sum_{ij} J(ij)\, (S^+(i)\, S^-(j) + S^-(i)\, S^+(j)), \tag{2}$$

where $I(ij)$ now refers to the zz tensor component and $J(ij)$ to the xx and yy components. Using the commutation relations for $S^{\pm}(\uparrow)$ and $S^{\pm}(\downarrow)$

where ↑ and ↓ refer to a spin up and a spin down sites respectively, we have (with $\hbar = 1$)

$$-i\,\frac{dS^+(\uparrow)}{dt} = [\mathcal{H}, S^+(\uparrow)] = -E_A\, S^+(\uparrow) + \sum_j I(j\uparrow)\, S_z(j)\, S^+(\uparrow) - \sum_j J(j\uparrow)\, S_z(\uparrow)\, S^+(j) \qquad (3)$$

$$-i\,\frac{d\,S^+(\downarrow)}{dt} = E_A\, S^+(\downarrow) + \sum_i I(i\downarrow)\, S_z(i)\, S^+(\downarrow) - \sum_i J(i\downarrow) S_z(\downarrow) S^+(i).$$

For $T \approx 0$, the spins are approximately aligned along the z axes so $|S_z(\uparrow)| = |S_z(\downarrow)| \equiv S$. If we assume each spin interacts only with its N next nearest neighbors, if $I(ij) = I = J$ (true for all except CoF_2), and if the spins have a sinusoidal time dependence $e^{i\omega t}$ and move in phase on each sublattice (true for $k = 0$), then the above equations reduce to:

$$\omega\, S^+(\uparrow) = -(E_A + NIS)\, S^+(\uparrow) - NIS\ S^+(\downarrow)$$

and

$$\omega\, S^+(\downarrow) = (E_A + NIS)\, S^+(\downarrow) + NIS\ S^+(\uparrow). \qquad (4)$$

If we set $NIS \equiv \mu H_E$ where H_E is the exchange "field" and $\mu = g\mu_B$ is the number of Bohr magnetons per spin, and if we set $E_{A_i} = \mu\, H_{A_i}$ where H_A is the anisotropy field, we obtain the familiar result for the AFMR:

$$\omega^2 = \mu^2\, (2\, H_E\, H_A + H_A^{\,2}). \qquad (5)$$

Equation (5) holds for k = 0, the region accessible to optical measurements.

2. Linear Chain Model

If we relax the assumption that all the spins move in phase but retain our other assumptions and our "field" notation, Eq. (4) may be modified to

$$\omega S_i^+(\uparrow) = \bar{\mu}\,(H_A + H_E)\, S_i^+(\uparrow) - \mu\frac{H_E}{N} \sum_{\substack{\text{next}\\ \text{nearest}\\ \text{neighbors}}} S_j^+(\downarrow)$$

and

$$\omega S_j^+(\downarrow) = \mu(H_A + H_E)\, S_j^+(\downarrow) + \mu\frac{H_E}{N} \sum_{\substack{\text{next}\\ \text{nearest}\\ \text{neighbors}}} S_i^+(\uparrow) . \qquad (6)$$

In this notation it is relatively simple to treat spin waves with k ≠ 0 propagating in a particular direction. We shall choose the direction ⊥ to the (011) (or equivalently the (110)) crystal plane to illustrate this method. Figure 2 shows that an (011) plane has two antiferromagnetically aligned sublattices a and b. Since the spin wave propagates in the (011) direction the spins on each sublattice of each plane perpendicular to the direction of the spin wave will be in phase. Therefore we need only to determine the equation of motion for one spin on each sublattice in each plane. We have reduced our problem to a one-dimensional chain of spins which are assumed to interact with each other in the same way as the actual sublattice spins interact. If there are N(011) planes in the crystal we need 2N spins in the chain--one for each sublattice. Figure 3 illustrates this chain.

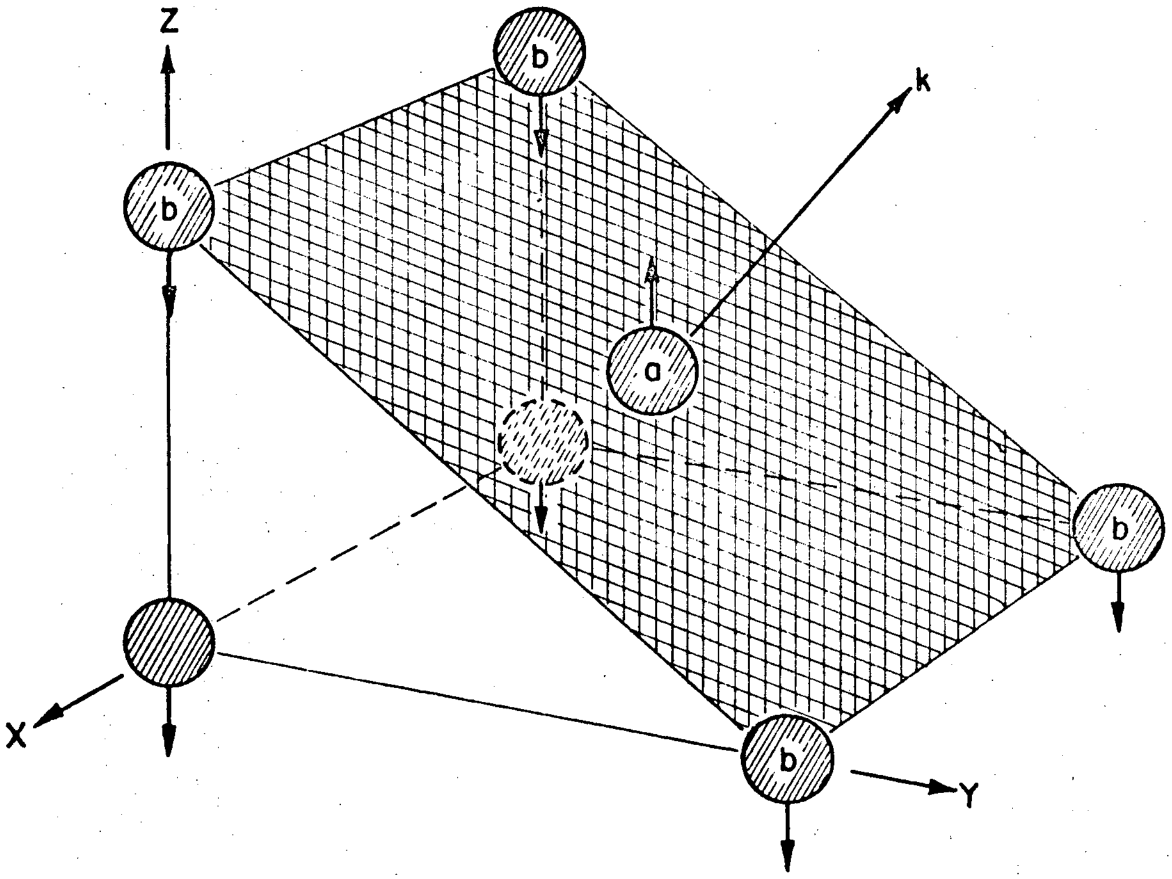

XBL 738-1616

Fig. 2. The (011) crystal plane in the rutile structure (cross hatched). The $\vec{k}$ vector of the propagating spin wave is shown ⊥ to plane. The plane is composed of two antiferromagnetically aligned sublattices, one consisting of "a" atoms and the other of "b" atoms. The spins on each sublattice in each plane move in phase but the spins on adjacent (011) planes will be out of phase.

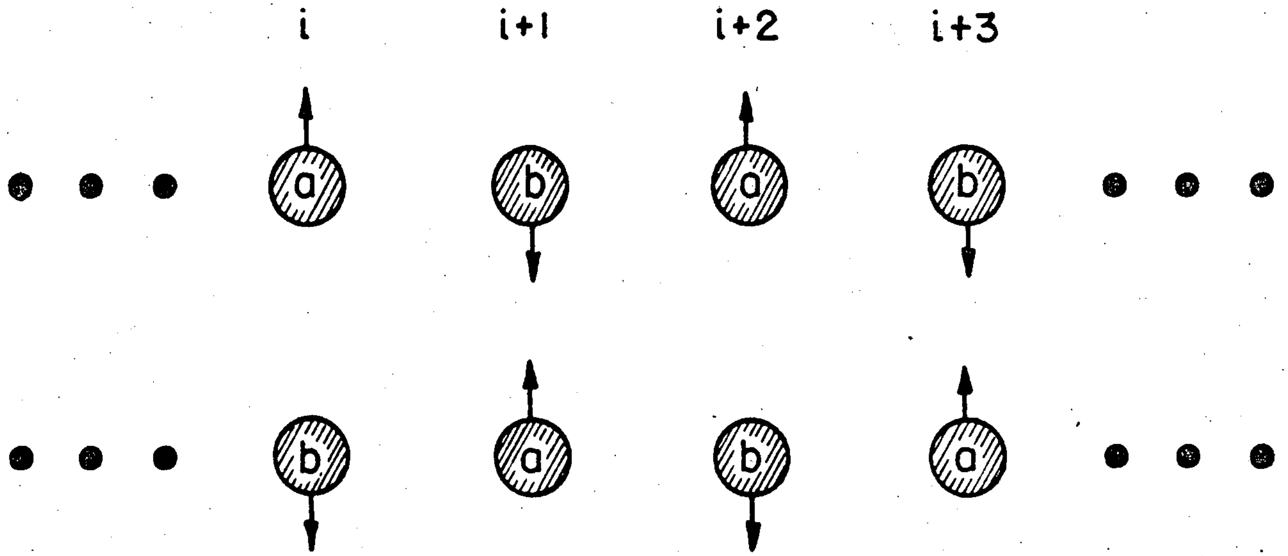

XBL738-1617

Fig. 3. The linear chain of ion pairs which represents spin waves travelling in the 011 direction. Each ion sees an anisotropy field H_A, an exchange field contribution $H_E/2$ from ions in the opposite sublattice of the same plane, and an exchange field $H_E/4$ from ions in the opposite sublattice of neighboring planes.

The equations of motion from Eq. (6) are

$$\omega S^{+}(a,i) = -\mu (H_A + H_E) S^{+}(a,i) - \mu\frac{H_E}{2} S^{+}(b,i) - \mu\frac{H_E}{4} (S^{+}(b,i-1) + S^{+}(b,i+1))$$

and

$$\omega S^{+}(b,i) = \mu (H_A + H_E) S^{+}(b,i) + \mu\frac{H_E}{2} S^{+}(a,i) + \mu\frac{H_E}{4} (S^{+}(a,i-1) + S^{+}(a,i+1)). \qquad (7)$$

By substituting a spatial variation of the form $e^{ik\alpha\Delta i}$ where k is a wave number and α is the separation between planes, we obtain

$$\omega^2 = \mu^2[(He + H_A)^2 - \frac{H_E^2}{16} (6 + 8 \cos k\alpha + 2 \cos 2 k\alpha)], \qquad (8)$$

which reduces to Eq. (5) for k = 0.

3. Molecular Field Approximation Demagnetization Effects and Resonance Intensity

There is an intuitive reason for defining H_E and H_A as we have done. If we return to Eq. (4) and define $\vec{\mu}_{\uparrow} = \mu\vec{S}(\uparrow)$, $\vec{H}_{E_{\uparrow}} = -H_E \frac{\vec{S}\downarrow}{|S\downarrow|}$, and $\vec{H}_{A\uparrow} = P_{\uparrow}H_A\hat{z}$, we find that the result is just the equation of motion of the x and y components of a dipole $\vec{\mu}_{\uparrow}$ in a magnetic field $\vec{H}_{E_{\uparrow}} + \vec{H}_{A_{\uparrow}} \equiv H_{\uparrow}$. Thus we may write for ↑ and ↓

$$\frac{d\vec{\mu}_{\uparrow}}{dt} = \mu\vec{\mu}_{\uparrow} \times \vec{H}_{\uparrow}, \quad \frac{d\vec{\mu}_{\downarrow}}{dt} = \mu\vec{\mu}_{\downarrow} \times \vec{H}_{\downarrow}. \qquad (9)$$

Or, if we sum over a unit volume:

$$\frac{dM_{\uparrow\downarrow}}{dt} = \mu\vec{M}_{\uparrow\downarrow} \times \vec{H}_{\uparrow\downarrow}. \qquad (10)$$

In this formalism, we can easily include the effects of demagnetization fields and applied fields. Let

$$\begin{aligned}\vec{H}_{\uparrow} &= \vec{H}_{E\uparrow} + \vec{H}_{A\uparrow} - \vec{\vec{N}}_{\perp}(\vec{M}_{\uparrow} + \vec{M}_{\uparrow})_{\perp} + \vec{H}_{o} \\ &= -\lambda\vec{M}_{\downarrow} + \vec{H}_{A\uparrow} - \vec{\vec{N}}_{\perp}(\vec{M}_{\downarrow} + \vec{M}_{\downarrow})_{\perp} + \vec{H}_{o}, \qquad (11)\end{aligned}$$

where H_o represents the applied field and $\vec{\vec{N}}_{\perp}$ is the demagnetization tensor in the $\hat{x}$ and $\hat{y}$ directions. We note that $H_{E\uparrow}$ is proportional to $M\downarrow$ and in the opposite direction. Moreover the demagnetizing field has no component in the z direction because of the cancelling effects of the oppositely oriented sublattices. The sublattice magnetizations, however, do not cancel in the perpendicular directions. We shall assume that $N_{\perp}$ is isotropic in the x and y directions.

For $H_o \parallel$ to the z axis and assuming $e^{-i\omega t}$ time dependence, the equations of motion yield at T = 0:[24,32]

$$\omega = \mu\left(\sqrt{2(H_E+N_{\perp}M)H_A+H_A^2} \pm H_o\right). \qquad (12)$$

For $H_o \perp$ to the z axis the following result is obtained

$$\omega = \mu\sqrt{2(H_E+N_{\perp}M)H_A+H_A^2 \pm H_o^2}. \qquad (13)$$

A further value of the molecular field approximation is seen in the determination of AFMR intensities. The Kramers-Krönig relation[33] imply that the integrated resonance intensity of a narrow resonance is proportional to the dc magnetic susceptibility times the resonant frequency ω_o. That is if

$$\chi_\perp''(\omega) = S\left(\frac{2\gamma/\pi}{\gamma^2+(\omega_o-\omega)^2}\right) \quad \gamma \ll \omega_o,$$

then

$$S = \frac{\pi}{2}\,\chi_\perp'(0)\;\omega_o, \tag{14}$$

where S is the resonance intensity $\chi_\perp''$ is the imaginary portion of the magnetic susceptibility, γ is the linewidth, and $\chi_\perp(0)$ is the dc susceptibility. Thus, we can compute the intensity of the AFMR by considering the dc susceptibility in a perpendicular field.

A field applied perpendicular to the spins will cause them to cant towards the applied field until the torques are balanced. Neglecting anisotropy fields and assuming that the canting angle θ is small, we have $2\,H_E\,\theta = H_o$ or $\theta = \frac{H_E}{2H_E}$. This $\Delta M_\uparrow = M_\uparrow\theta = \frac{M_\uparrow H_o}{2H_E}$, and the total for both sublattices gives

$$\chi_\perp' = 2\,\frac{\Delta M\!\uparrow}{H_o} = \frac{M}{H_E}\,. \tag{15}$$

From Table I, we have $H_E = 2.5 \times 8 \times I(2) \times \frac{1}{\mu} \approx 500$ kG and $M_S \approx 600$ G which says that $\chi_\perp' \approx 10^{-3}$, or about 2.5×10^{-4} emu/gm, which is the value given in the table. The intensity of the AFMR is thus $\approx 10^{-2}$ cm^{-1}.

4. Usefulness of Different Theoretical Methods

Thus far we have presented three approaches to antiferromagnetic resonance each of which is useful for solving a particular type of problem. The basic Heisenberg approach is helpful when considering defects since it is readily adaptable to Green's function techniques. The molecular field approximation, as we have seen, permits a natural treatment of macroscopic magnetic field effects, and the linear chain model is the most convenient approach when considering surface antiferromagnetic resonance modes (SAFMR modes) which are uniform along planes parallel to the surface but attenuate as they penetrate into the bulk.

C. Experimental Apparatus and Techniques

Both Fourier-transform spectroscopy and high frequency microwave techniques have been employed to study the transmission of the iron-group fluorides in the far-infrared. We shall describe the Fourier transform apparatus first.

1. Fourier Transform Spectroscopy

To facilitate our description, we shall trace the path of energy from its blackbody source through the interferometer and sample to the detector, and we shall trace the detected signal through the electronics to the output spectrum. Both the interferometer and the cryostat used have been described elsewhere.[34] A schematic of the Michelson interferometer is given in Fig. 4.

a. The far-infrared source. The Hg arc temperature was nominally 3000K. The source output was collimated by a parabolic mirror (F 1.5). The total signal power per unit frequency is given by the expression $P(\nu) = 2k_B \Delta T c \nu^2 A\Omega$, where ν is in cm^{-1} and ΔT = ((source temperature)-(room temperature)). For this system $2k_B \Delta T c A\Omega$ was 5×10^{-11} $w\text{-}cm^3$.

b. The beamsplitter. Mylar sheets stretched on aluminum frames and annealed to improve flatness were used as beamsplitters. The sheets used varied in thickness from 1/2 mil to 5 mils, depending on the frequency range of interest. The efficiency ($\varepsilon(\nu)$) of these beamsplitters typically varied as $\sin^2\nu$ (from Fabry-Perot interference effects) reaching a maximum of about 70%.

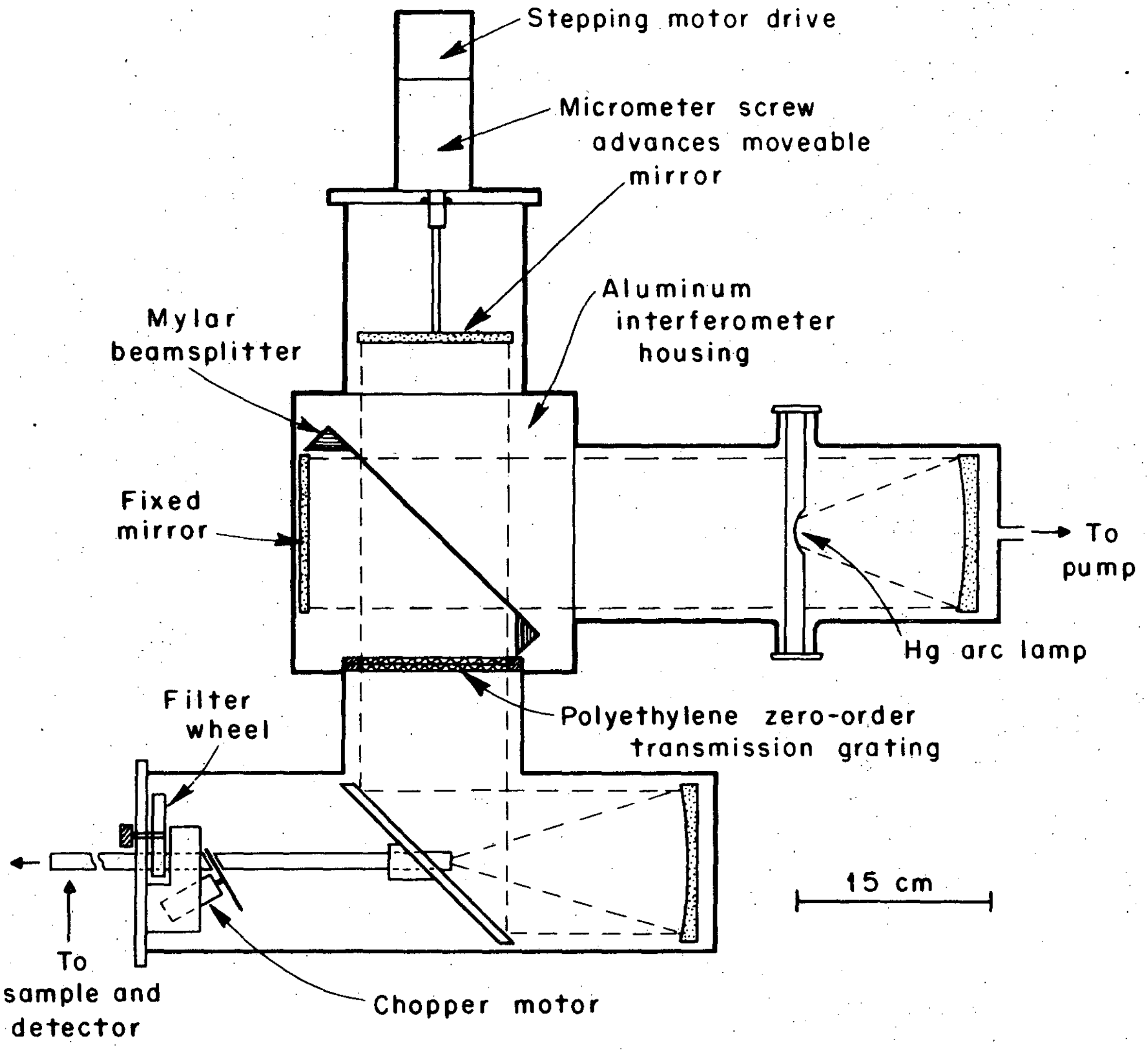

XBL682-2036-A

Fig. 4. A schematic of the michelson interferometer.

c. The mirrors. Each of the two beams from the beamsplitter was reflected by a mirror. The fixed mirror could be tilted slightly by two orthogonal adjustments to align the optics of the interferometer. The movable mirror was mounted on a shaft attached to a micrometer screw. This screw was turned through a 6:1 reduction gear by a stepping motor. The combination of reduction gear and micrometer screw permitted the stepping motor to advance the movable mirror by an increment of 1/24,000 cm. The maximum distance of mirror travel was 4 cm from zero path giving a maximum path difference between the beams of 8 cm.

d. The polyethylene zero order transmission grating. This grating consisted of two ruled sheets of polyethylene crossed at right angles to each other and placed in the beam. When used, this grating diffracted light above 25 cm^{-1} out of the beam emerging from the beamsplitter.

e. The chopper and motor. After the emerging beam had been refocused into lightpipe by a second parabolic mirror, it was chopped by a two bladed chopper (turned by a synchronous motor at ≈ 40 Hz) to permit lock-in detection.

f. Yoshinaga filters. A filter wheel containing filters with a variety of high frequency cutoffs was used to help select the frequency range for spectral examination. These filters were made from powdered alkali-halides suspended in polyetheline.[33]

g. The emergent beam. The average chopped intensity of the emergent beam is given by

$$I(\Delta) = 1/2\int_{0}^{\infty} S(\nu)\ \left(\frac{1+\cos 2\pi\Delta\nu}{2}\right)d\nu, \qquad (16)$$

where $S(\nu) = P(\nu)\varepsilon(\nu)F(\nu)$, $F(\nu)$ is the transmission characteristic of the high frequency cutoff filter and Δ is the path difference between the two halves of the split beam. Note that for large Δ the cosine term averages to zero and $I(\Delta)$ is a constant.

The emergent beam from the Michelson entered a cryostat which held the sample and bolometer at LHe temperatures. Figure 5 shows the more elaborate of the two cryostats used. Light was transmitted from the Michelson through a thin layer of black polyethylene through the light-pipe and a focusing cone, and finally through the sample and a de-focusing cone onto the bolometer.

h. <u>Cold filters</u>. A piece of black polyethylene (500 cm^{-1} cutoff) or a piece of fluorogold (50 cm^{-1} cutoff) usually was placed in the liquid helium above the bolometer to screen out unwanted room temperature background radiation. Fluorogold consists of teflon impregnated with small glass beads and is obtained from the Fluorocarbon Company, Mountain View, California.

i. <u>Samples</u>. All samples were mounted in small brass cylinders 7/16" o.d. × 3/16" i.d. × 0.465" long. For large and irregularly shaped single crystals, the sides of the cylinders were cut away to insert the crystal. If necessary, aluminum foil was placed around the crystal to reflect light scattered through the side of the crystal back into the beam.

j. <u>The magnet</u>. The superconducting NbZr magnet had a nominal field-to-current ratio of 3.48 kG/A and a maximum field strength of over 50 kG. The field-to-current ratio was verified by observing the microwave absorption of DPPH ($g = 2.00$) at 74.74 GHz. The observed field-to-current ratio was 3.49 ± 0.25 kG/A. On several occasions during the microwave

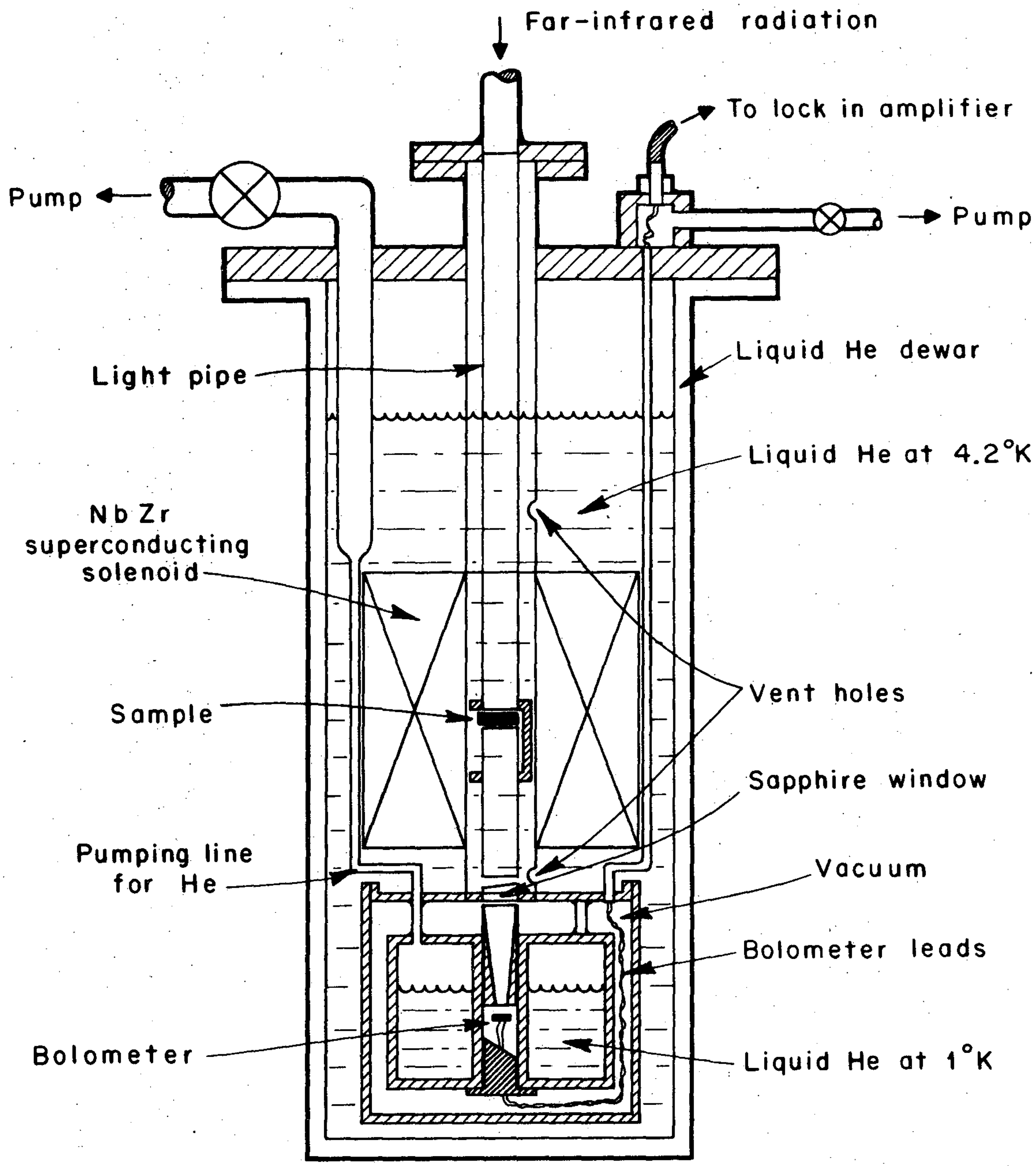

XBL 682-2034-A

Fig. 5. The superconducting magnet cryostat.

experiments, a magnetoresistance probe, consisting of several feet of #41 insulated Cu wire wound on a wooden stick and measured by a four-terminal circuit was inserted in the magnetic field and monitored as the field was increased to 45 kG. No sudden changes in slope or discontinuities indicating defects in the magnet were observed. These tests were made to insure that the magnet operated properly in a continuous field sweep mode. This same magnet had been used extensively for fixed-field applications and was known to perform well.

When the field of the magnet was turned up, the bolometer gave an extremely noisy response for currents up to about 4 A. These fluctuations were typically on the order of 10 μV (but occasionally as large as 100 μV) and of duration equal to the lock-in response time of 0.1 sec. The product of a typical observed voltage spike with the response time yields a flux of 10^2 G cm^2, which corresponds to a field change of 10^2 G in a bolometer circuit of 1 cm^2 area. It appears then, that flux jumping in the magnet is a probable source of this noise.

k. The bolometer. A germanium bolometer [35,36] was used to detect the emergent far infrared radiation from the sample. A fundamental measurement of bolometer sensitivity in any given electrical circuit is its noise equivalent power (NEP). The NEP is defined as the amount of signal power incident on the detector required to produce a response at the output of the amplifying circuit equal to the rms noise at the amplifying circuit output. NEP is usually given in $W\sqrt{Hz}$. The NEP for this bolometer was nominally $\approx 10^{-12}$ $W\sqrt{Hz}$.[37] The bolometer could detect Johnson noise in a 9 MΩ room temperature bias resistor. The signal-to-noise ratio at $\Delta = 0$ for radiation from the Michelson with a 25 cm^{-1} cutoff was ≈ 1500 with a one-second lock-in time constant. Using Eq. (16) and the measured signal-to-noise ratio, and allowing a factor of ≈ 10 for attenuation due to optical filters, lightpipe and electronic filtering in the lock-in (due to chopping and rounding off the input square wave), we compute a minimum detectable signal of $\approx 10^{-12}$ W for a one-second time constant, which agrees with the nominal value.

ℓ. Alternate cryostat. For runs in which it was not necessary to have the highest signal-to-noise ratio, and in which no applied magnetic field was needed, a glass cryostat was used. The insert for this apparatus had a rotating cylinder which held six samples, any one of which could be rotated into the far infrared beam without recycling the apparatus to room temperature. The operating temperature was ~ 1K. No specific study was made of the NEP of the bolometer in this apparatus. It was found, however, that the bolometer responsivity tended to drift (possibly due to the falling LHe level in the cryostat). These drifts were not a serious problem since data could be taken rapidly enough to avoid significant variation over the space of a single interferogram. The coadding capacity of the computer permitted several interferograms to be averaged together to increase the signal-to-noise when necessary.

m. Signal detection and digitizing. The bolometer signal was detected by a low-noise, high-impedance lock-in detector. The output of the lock-in entered a voltage-to-frequency converter (VFC) whose output was counted and fed into the PDP-11 digital computer. The counting noise in the VFC was ≈ 17 counts (out of $\sim 10^4$ counts), and thus it was necessary to adjust the gains in the system to insure that the magnitude of the signal was much higher than the counting noise.

n. The PDP-11 computer. The PDP-11 on line digital computer could store interferograms up to 1024 points long. The capabilities of this machine were: real-time computation and display of spectra, apodization of spectra, phase correction of spectra, co-adding of spectra or interferograms, ratioing of spectra, and computation of absorption coefficient from ratios of spectra. Display options included an x-y plotter and a storage oscilloscope. Data were also punched out on paper tape.

o. Method of operation. Our interferograms were measured by a step, pause, and count technique. After the computer had recorded a data point, it issued a signal to the stepper motor in the Michelson to advance the movable mirror by a fixed amount Δ. After each advance there was a pause to allow electrical transients to die away before the next data point from the Vidar was counted. This pause was equal to five lock-in time constants. The Vidar output was counted for a fixed integration time (usually 1-4 seconds).

p. Resolution limits on the spectrum. The peculiar properties of Fourier transform spectroscopy have been discussed elsewhere[33,38] and only a brief discussion will be given here. The power absorbed by the bolometer $I'(\Delta)$ is given by an expression identical to Eq. (16), except $S'(\nu)$ now includes the sample spectrum multiplied by the instrumental spectrum $S(\nu)$:

$$I'(\Delta) = 1/4\int_0^\infty S'(\nu)(1+\cos(2\pi\nu\Delta))d\nu. \qquad (17)$$

To retrieve $S'(\nu)$, one performs an inverse cosine transform on $I'(\Delta)$:

$$S'(\nu) = 4\int_0^\infty (I'(\Delta) - 1/2\ I(0))\cos(2\pi\nu\Delta)d\Delta. \qquad (18)$$

If $I'(\Delta)$ is not known to infinite Δ but only to some maximum path difference L, the above integration can only be taken out to L. This is equivalent to multiplying the integrand of Eq. (18) by the function

$$W(\Delta) = \begin{cases} 1 \text{ for } \Delta \leqslant L \\ 0 \text{ for } \Delta > L \end{cases}. \qquad (19)$$

The resultant spectrum will be the convolution of $S'(\nu)$ with the Fourier transform of $W(\Delta)$ which is the sinc function $(4\ \frac{\sin 2\pi L\nu}{2\pi\nu})$. This convolution has the effect of broadening sharp lines to a width of $\delta\nu_{min} = 1/2L$, the width of the central maximum of sinc x. $\delta\nu_{min}$ is called the "resolution" of the spectrum. One disadvantage of the sinc function is that it has large positive and negative side lobes neighboring the central maximum which tend to introduce spurious sharp fluctuations into the spectrum. These fluctuations may make it difficult to identify a small sharp spectral feature.

To reduce the effect of the side lobes in the sinc function the technique of apodization may be used. This consists of replacing $W(\Delta)$ by a smoothing function, in our case by

$$A(\Delta) = \begin{cases} 1 - \Delta/L \text{ for } \Delta \leqslant L \\ 0 \qquad\quad \text{ for } \Delta > L \end{cases}, \qquad (20)$$

whose transform, sinc^2, has small, positive side lobes. This is done at the cost of some resolution since $\delta\nu_{min} \approx 3/4L$ for the sinc^2 function.

q. Sampling considerations. Our interferograms were sampled periodically as described above. Elementary sampling theory states that no spectral information is lost by this periodic sampling provided that the highest non-zero frequency in the spectrum, ν_{max}, is less than or equal to $1/2\Delta$ where Δ is the incremental change in path length. In an N point interferogram, L is equal to $N\Delta$, so the relation between $\delta\nu_{min}$ and ν_{max} for an unapodized spectrum is

$$\delta\nu_{min} = \frac{\nu_{max}}{N} . \tag{21}$$

The spectral transform may be approximated by a summation

$$S'(\nu) = 2\Delta \left(\frac{I(0)}{2} + \sum_{n=1}^{N} I(N\Delta) \cos(2\pi\nu n\Delta)\right). \tag{22}$$

There will be noise $\theta(n\Delta)$ associated with each point on the interferogram so that the actual computed spectrum is

$$S_c(\nu) = 2\Delta\left(\frac{I(0)}{2} + \sum_{n=1}^{N} [I(n\Delta)+\theta(n\Delta)] \cos 2\pi\nu n\Delta\right). \tag{23}$$

Squaring the above equation gives

$$S_c(\nu)^2 = S'(\nu)^2 + (2\Delta)^2 \frac{N}{2} \theta_r, \tag{24}$$

where θ_r is the ms noise on one point of the interferogram. Thus the ms noise on a point of the spectrum is

$$\theta_s = \frac{N}{2}\,\theta_r\,(2\Delta) = \frac{N}{2}\,\frac{\theta_r}{\nu_{max}}\,. \tag{25}$$

Our best signal-to-noise value for a ratio of spectra computed from a 400 point interferogram was about 50:1, which is consistent (within a factor of 2) with the measured value of bolometer signal-to-noise at zero path.

It is interesting to note that θ_r is proportional to $\frac{1}{\sqrt{\tau}}$ where τ is the counting time per point. The total counting time $T = N\tau$ is a measure of the time required to take an interferogram. θ_s can be rewritten as

$$\theta_s = \alpha\,\frac{N}{\sqrt{2N\tau}}\,\frac{1}{\nu_{max}} = \frac{\alpha}{\nu_{min}\sqrt{2T}} \tag{26}$$

where α is a constant depending on the instrumental sensitivity. Thus, for a fixed amount of spectral noise, spectral resolution can be increased (ν_{min} decreased) only at the cost of a quadratic increase in the total time for data collection.

2. Microwave Apparatus

The microwave apparatus was used only in the surface magnon investigation. Figure 6 gives a schematic of the experimental setup.

a. Source. A V-band klystron operating at 75 GHz was used to generate ≈ 20 mW of monochromatic radiation. The klystron was modulated at ≈ 200 Hz by the square wave modulator in the power supply. The radiation leaving the klystron was attenuated to adjust the power to desired levels.

b. E-H tuner. Following the attenuator was an E-H tuner which consisted of a magic tee with each branch arm of the tee (those perpendicular to the input waveguide) terminating in a reflector whose position was adjustable. By adjusting these reflectors it was possible to null the output signal (emerging from the fourth arm of the tee). By measuring the distance between nulls it was possible to determine the guide wavelength (and hence the frequency) of the incident radiation (to better than 1% accuracy).

c. Magic tee. Following the E-H tuner a magic tee was used to make the right angle bend downward toward the cryostat. The upward branch of the tee provided a monitoring port for the klystron output.

d. Harmonic generator. A semiconductor point contact diode served as the required non-linear element to generate the second harmonic of the klystron frequency. Approximately 1 μW of 150 GHz microwaves left the generator through F-band waveguide which effectively screened out the klystron fundamental. The generator also doubled as a detector of the fundamental klystron power.

e. The cryostat insert. The output of the harmonic generator was coupled into a length of V-band guide which had been soldered into a brass flange to form an insert for the magnet cryostat described above. The lower end of this insert extended down to a level even with the top of the magnet, a layer of black polyethylene was clamped between microwave flanges at the top of the insert to prevent cryopumping of air down the guide.

f. Different shapes of waveguide used to hold the oriented crystal samples were attached to the lower end of the flange. For large single crystals it was necessary that the surface of interest be parallel to the side of the waveguide and that the c-axis be parallel with the applied magnetic field. For the crystals with (110) faces and for powders (which require no special orientation) a straight length of guide was used. For the (111) face crystals, however, it was necessary to build the curved guide shown in the inset of Fig. 6.

g. Microwave detection. The microwaves emerging from the sample were matched to lightpipe by a horn and detected by the germanium bolometer described above.

h. Mode of operation. The superconducting magnet power supply was swept continuously by a geared synchronous motor from ≈ 0 A to ≈ 14 A (corresponding to ≈ 49 KG) at a rate of 1.4 A/min. This rate was set for experimental convenience. The bolometer response was plotted vs current from the power supply on an x-y plotter. Absorption was seen as a decrease in the bolometer response as a function of magnetic field (or current). We note that due to the long time constant formed by the magnet inductance and the shunt resistor, the change in current in the magnet itself generally lagged behind the change in magnet supply current. This caused an ≈ 1-2% shift in plotted absorption features. The direction of the shift depended on whether the current was being increased or decreased.

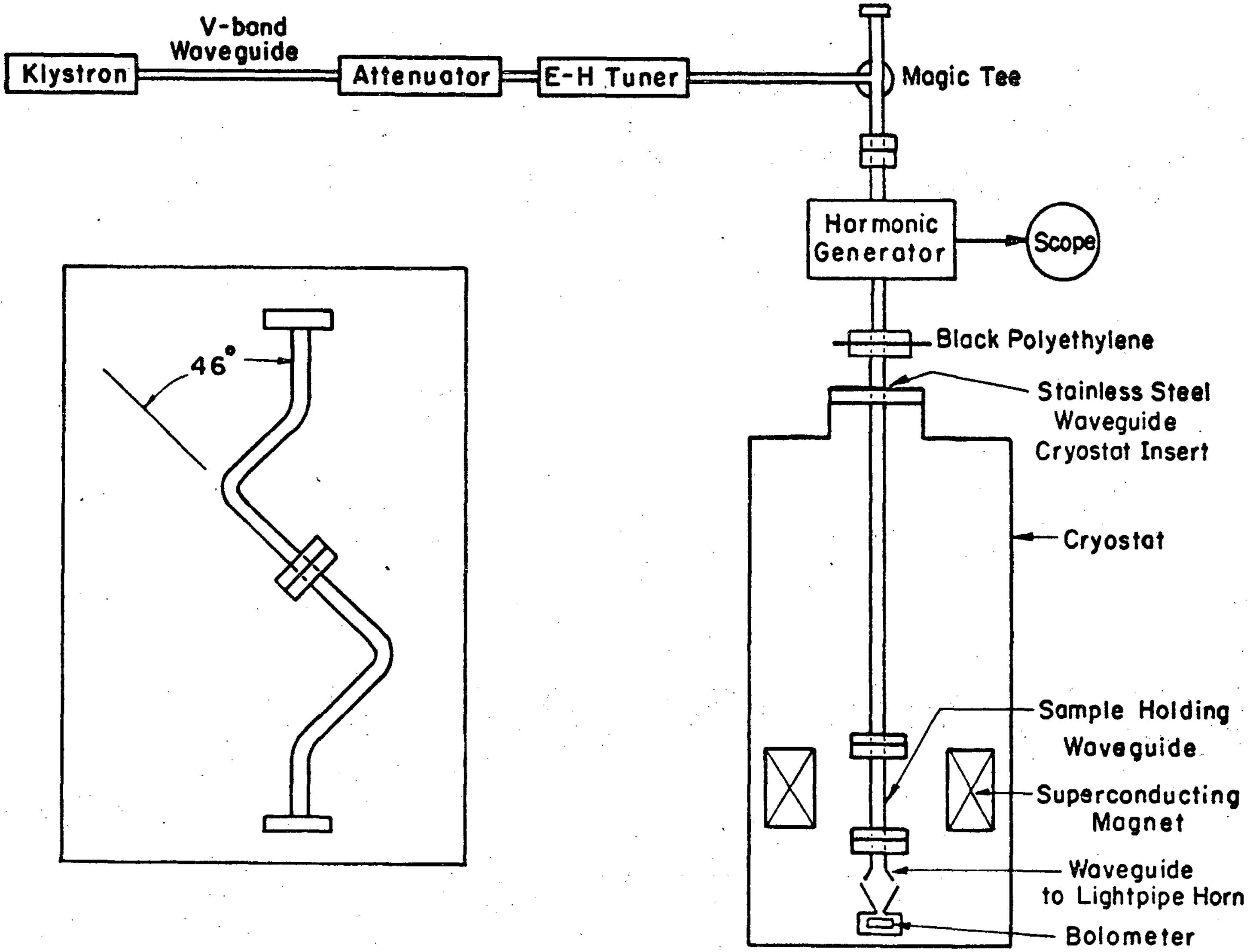

XBL 744-6185

Fig. 6. Schematic diagram of microwave apparatus. The insert depicts curved waveguide sections used to hold crystals with (111) plane surfaces in the proper alignment with the magnetic field. This curved waveguide was used in place of the straight waveguide sample holder shown in the figure outsert.

CHAPTER II. POSSIBLE SURFACE ANTIFERROMAGNETIC RESONANCE (SAFMR OR SURFACE MAGNONS)

Surface magnetic resonance effects in antiferromagnets have been predicted by Mills and Saslow[39], and by Wolfram and De Wames.[40] The predicted mode frequencies lie below the antiferromagnetic resonance by varying amounts depending on the crystal structure, the Miller indices of the surface, and the exchange and anisotropy parameters of the crystal. Until now, there has been no direct observation of these surface antiferromagnetic magnon modes, although surface phonon and plasmon modes are well known.[41-43] We have observed two modes in addition to the AFMR, both of which lie between the two published theoretical results for surface magnons. Each mode shows some of the characteristics of a surface magnon mode.

Both microwave techniques and Fourier transform spectroscopy have been used to study these extra magnon modes in MnF_2. The Fourier transform techniques have been used primarily on powder samples whereas the microwaves have been used mainly in single crystal studies.

A. Far-Infrared Experiments

1. Sample Preparation

Three single crystals of MnF_2 were obtained from two different sources. The two crystals supplied by Dr. E. Catalano at the Lawrence Livermore Laboratory were the source of all but two of the samples made. Both of these crystals are known to contain impurities of a non-magnetic nature. The larger single crystal was brown rather than pink due to the presence of oxygen, which was accidentally admitted into the melt before the crystal was formed. The smaller crystal from Catalano, although it had the normal pink color, showed three strong, broad absorptions in the far IR at 23.5, 31, and 49.5 cm^{-1}. These absorptions did not change measurably in an applied magnetic field of ≈ 16.5 KG. Moreover, emission spectroscopic analysis of these samples showed no magnetic impurities in the pink sample and only .01% Fe and .05% Ni in the brown sample. Both samples showed the strong AFMR at 8.7 cm^{-1}, and it was assumed that the impurities played no significant role in the antiferromagnetic properties of these samples.

To make absolutely sure of our experimental results, however, a third single crystal of nominally high purity was obtained from Dr. R. Macfarlane at IBM, San Jose. This crystal had both the proper color and no extra infrared absorptions. Both emission spectroscopy and exciton fluorescence analysis of this sample done by Macfarlane showed no cation impurities greater than one part in 10^4.

The single crystal samples used for infrared experiments were oriented by X-ray back reflection after first being roughly oriented by eye using polarized light. Samples were cut to size by a diamond saw and then re-oriented by X-rays and ground smooth with #600 grit silicon carbide paper. All samples were ground with at least one surface within 3° of the 001 plane for orientation in a magnetic field. This orientation was not considered critical, however, since we were not attempting to measure magnetic field effects but only to observe the presence of extra magnetic absorptions in zero field. The samples were secured by parawax into the cylindrical brass holders described above. Total alignment of the c-axis with the axis of the cylinder and light pipe was estimated to be within 10°, and thus adequate for our purposes.

Powder samples were ground from the single crystal with an agate mortar and pestle. The powders were sieved to give some segregation according to grain size. The coarsest grind sample passed through a sieve whose square holes were 233 μ on a side, but not through a 159 μ sieve; the medium grind through 159 μ, but not 85 μ; and the finest grind through 47 μ. Each sample was then tamped into one of the cylindrical brass holders which had first been cleaned with acetone. The tamped samples were then saturated with melted parawas (index of refraction ≈ 1.5) to hold them together and provide some index matching for incident radiation. 273 mg samples were made from all three grinds and 68mg samples only from the coarse and fine grinds. Three samples were prepared somewhat differently from the above manner. One sample of the finest powder grind was diluted with ten times as much ZnF_2 powder of an equally fine grind. The two powders were sifted together through the 47μ sieve used to determine the powder grind originally. This had the effect of reducing the fractional volume occupied by the magnetic powder to 1/11 of the original. To hold this sample, a longer brass cylinder with the same diameters was used.

The second special sample was of the coarse powder grind and was tamped into a brass cylinder blocked at the bottom by a parawax plug. A second plug was pressed into the top of the cylinder to hold the sample together. This sample, however, was not immersed in parawax.

The last specially prepared sample was a coarse grind sample, warmed to 500°C from room temperature over about 5 hours, annealed at ≈ 500°C for about 1 day, and then cooled slowly to room temperature over about a one-day period. Maximum pressure during annealing was $\approx 3 \times 10^{-6}$ Torr.

This sample was made from the starting material which contained oxygen and weighed > 300 mg before annealing. After annealing the powder was greyish white rather than brownish white, and weighed 166 mg. The only way we could think of to account for the apparent loss of weight is to assume that some of the powder was spilled or that the weight before annealing was not measured correctly. The change in color may possibly have been caused by the oxygen in the sample or by the residual gas pressure in the annealing furnace. The absorption strength of the AFMR in this sample, however, showed that the amount of MnF_2 present was in the same proportion to the sample weight as an unannealed sample of the same grind and so the results in the far-IR are assumed to be valid.

2. Powder Surface-to-Volume Ratio

The resonance intensity of a surface magnon should be proportional to the surface area of the crystal face on which that resonance appears. In a powder sample we would expect the surface area associated with any particular crystal face formed in the grinding process to be proportional to the total surface area of the powder. This assumption should be closer to the actual situation for the finer grinds because proportionately less of the original surface associated with the uniquely shaped starting crystal is left. Furthermore, on a microscopic level we would expect that most of the powder particle surface area will be composed of cleavage planes since the crystallites break preferentially along these planes. Even surfaces which appear to be significantly different from the cleavage plane, may have a cleavage plane "step" structure on the scale of several lattice spacings.[44]

Because the surface area is proportional to surface magnon intensity, it is important to be able to measure both the absolute and the relative surface area of the different powder sample grinds. The powder samples all have the same volume so the surface-to-volume ratio of the powders is proportional to the surface area. The surface-to-volume ratio (SVR) is a function of both particle shape and size. If the particle is an ellipsoid, or rectangular solid, the SVR is given by

$$\mathrm{SVR} = \frac{2ab + 2bc + 2ca}{abc} , \tag{27}$$

where a, b, and c are the major, intermediate, and minor axes of the particles. Prisms and other similar convex shapes with the same length axes may have higher values of SVR by as much as a factor of 2.

Assuming that the distribution of shapes is the same for different powder grinds, the variation in shape should not affect our estimate of the relative SVR's. Similarly, we can ignore possible surface pitting effects on the relative SVR's since these, too, should be the same on all surfaces regardless of particle size. In fact, surface pits or bumps cannot give a very great error even in our absolute estimate of surface area. Therefore, if we treat the particles as if they were all rectangular solids, we shall introduce an error of ≈ 2 or less in our estimate of the surface area. This error will be on the low side of the actual value.

Assuming that the minor axis of each crystallite is perpendicular to the microscope slide on which the powders are placed, it is possible to measure a random sample of major and intermediate axes with a microscope.

With the larger crystallites, it is even possible to measure a random sample of minor axes by focusing on the bottom and top of each crystallite and measuring the height difference from the calibrated microscope dial.

From Eq. (27), it is a simple matter to see that the average SVR for a particle in the powder is just $\left(\overline{\frac{2}{a}}\right)+\left(\overline{\frac{2}{b}}\right)+\left(\overline{\frac{2}{c}}\right)$. However, this is not the SVR which is relevant to our problem. The relevant SVR is that of the powder as a whole (or of a statistical sample thereof) which is a measure of the surface area. In general, this SVR depends on correlations between axes and will not necessarily be equal to the mean particle SVR just as the average of reciprocals does not in general equal the reciprocal of the average.

The surface-to-volume ratio of the powder depends on the probability distribution of axes. There are two extreme cases: (1) the particles all have the same shape--that is, if a, b, and c are major, intermediate and minor axes of any crystallite then $a:b:c = \alpha:1:\gamma$ where α and γ are positive real numbers and $\alpha \geqslant 1 \geqslant \gamma$. (2) There is no correlation between crystal axes--that is, the probability $P(r_1)$ that the first axis measured has a length (r_1) is independent of the lengths of the other two axes. (Note in (2) that r_1 may be any of the principal axes, not necessarily the major axis.) In a real powder we expect that there will be some correlation between lengths of axes. The grinding process in a nearly cubic material will tend to preferentially break very long thin crystals and very broad, flat ones. Therefore, we would not expect to find many crystallites with axes of greatly different lengths. On the other hand, the sifting process separates out only those particles which have at least two axes which can pass through the coarser screen and two which cannot pass through the finer. Thus, sifting tends to segregate particles according to their intermediate length axes. We shall analyze these two extreme cases and assume that our powders lie somewhere in between.

We first consider the correlated case. Let P(abc) be the probability of finding a crystallite with major axis a, intermediate axis b, and minor axis c.

In order to normalize P let $\int_0^\infty P(abc)\, dadbdc = 1$, then

$$SVR = 2\,\frac{\int_0^\infty P(abc)(ab+bc+ac)\,dadbdc}{\int_0^\infty P(abc)\; abc\; dadbdc}\;. \qquad (28)$$

Let $P(abc) = P(b)\;\delta(\alpha b - a)\;\delta(\gamma b - c)$ where P(b) is a peaked distribution with average T_o and width Δb which we shall approximate by the function

$$P'(b) = \begin{cases} 0 & b < \bar{b} - \Delta b/2,\; b > \bar{b} + \Delta b/2 \\ \frac{1}{\Delta b} & \bar{b} - \Delta b/2 \leqslant b \leqslant \bar{b} + \Delta b/2 \end{cases}\;. \qquad (29)$$

Substituting into Eq. (28), we find

$$SVR = 2\;\left(\frac{1}{\alpha} + 1 + \frac{1}{\gamma}\right)\;\left(\frac{\int P'(b)\;b^2 db}{\int P'(b)\;b^3 db}\right.$$

$$= 2\;\left(\frac{1}{\bar{a}} + \frac{1}{\bar{b}} + \frac{1}{\bar{c}}\right)\;\frac{12+(\Delta b/\bar{b})^2}{12+3(\Delta b/\bar{b})^2}$$

$$\approx 2\;\left(\frac{1}{\bar{a}} + \frac{1}{\bar{b}} + \frac{1}{\bar{c}}\right)\quad \text{for } \Delta b \leqslant \bar{b}. \qquad (30)$$

The uncorrelated case is simpler. Let $P(r_1)$ be the probability of finding the first axis measured to have length r_1. $P(r_1r_2r_3) = P(r_1)P(r_2)\;P(r_3)$

and $\int P(r_1 r_2 r_3)\, dr_1 dr_2 dr_3 = 1$. We have

$$\mathrm{SVR} = 2\,\frac{\int_0^\infty P(r_1 r_2 r_3)(r_1 r_2 + r_2 r_3 + r_3 r_1)\, dr_1 dr_2 dr_3}{\int_0^\infty P(r_1 r_2 r_3)\, r_1 r_2 r_3\, dr_1 dr_2 dr_3}$$

$$= \frac{6}{\int_0^\infty P(r_1) r_1} = \frac{6}{\bar{r}} = \frac{18}{\bar{a}+\bar{b}+\bar{c}}\,, \tag{31}$$

since $\bar{r} = \frac{\bar{a}+\bar{b}+\bar{c}}{3}$. In the case of powders for which $\bar{a} < 2\bar{b}$ and $\bar{c} > \frac{1}{2}\bar{b}$ (as is the case with our powders), the difference between Eq. (30) and Eq. (31) is less than 40%. For convenience, we shall use the result of Eq. (31) to compute the SVR for our coarser grind powders, and expect the result to be somewhat low because the powders are somewhat correlated.

The finest grind powder grains are too small to measure $\bar{c}$. Moreover, this powder was sifted differently from the other two, having not been passed through a fine screen to eliminate the smallest particles. Using the uncorrelated axis approximation on the two smaller axes of this sample, we may obtain an estimate of the average value of the minor axis from the observed distribution of the intermediate axes.

Let P(r) be the probability that the first measured smaller axis (assuming both could be measured) has the value r. The observed distribution of smaller axes will have the value

$$P_o(r) = P(r) \int_o^r P(r')\, dr'. \tag{32}$$

This says simply that, of the two smaller axes of a crystallite, the larger one is observed. Letting $\int_o^r P(r')dr' = \pi(r)$, we have from Eq. (32)

$$\left(\frac{d\pi(r)}{dr}\right)\pi(r) = P_o(r)$$

$$\frac{d}{dr}\left(\frac{\pi(r)^2}{2}\right) = P_o(r)$$

$$\pi(r)^2 = 2\int_o^r P_o(r)$$

$$\pi(r) = 2\int_o^r P_o(r)$$

$$P(r) = \frac{P_o(r)}{2\int_o^r P_o(r)dr} \quad . \qquad (33)$$

When applied to a histogram of the fine particle grain size distribution, this formula shifts the actual small axis average down by about 10% from the observed small axis average. That is

$$\bar{r} = \int r\ P(r)dr = .9 \int rP_o(r)dr. \qquad (34)$$

$\bar{r}$ is the average value of both small axes so $\bar{r} = \frac{\bar{b}+\bar{c}}{2}$. The measured value of $\bar{a}$, $\bar{b}$, and $\bar{c}$ for the three particle grinds is given in Table 3 along with the surface to volume ratio computed from Eq. (31).

We conclude that we are able to measure the relative surface-to-volume ratio of the different powders to within about 50% (30% from the standard deviation of the measurement and 20% for possible axis correlations in the coarser grind powders which are not present in the finer grind because the latter was not sifted by a second screen). The absolute measure of surface-to-volume ratio is estimated to be within a factor of 2.

Table 3

Sample	$\bar{a}(\mu)$	$\bar{b}(\mu)$	$\bar{c}(\mu)$	SVR(cm^{-1})
coarse	387 ±91	227 ±47	118 ±37	246 ± 37
medium	327 ± 83	165 ± 25	83 ± 27	313 ± 49
fine	52 ± 17	25 ± 10	25 ± 10	1765 ± 454

Errors shown are computed using the standard deviations of the measured averages. The total area of the finest grind powder A = V × SVR is about 100 cm^2.

3. Results

Far infrared transmission spectra of the coarse and intermediate grind powder samples described above showed two absorptions, one at 8.3 cm^{-1} and the other at 7.7 cm^{-1}, in addition to the AFMR at 8.7 cm^{-1}. The lowest frequency mode was considerably reduced in intensity in the intermediate grind of powder. In the finest grind of powder, only the 8.3 cm^{-1} mode appeared. Neither mode appeared in single crystals of the same material. Both modes were quite sharp, in every case being narrower than 0.1 cm^{-1} and thus unresolved by our spectrometer. Figure 7 shows transmission spectra taken of 273 mg samples of three different powder grinds. These spectra have been ratioed either to a spectrum of a ZnF_2 powder sample, or to a spectrum of a blank sample holder to remove instrumental background effects. In this frequency range, no significant difference was observed between ratios to ZnF_2 and ratios to the empty sample holder. Because of the high index of refraction of MnF_2 ($n \approx 2.5$), the coarsest powder had particles with dimensions on the order of the wavelength of the incident light. As a result, powder scattering reduced the transmission through this sample causing a larger fractional noise to appear on the ratio. Note also that, because of the smaller signal at the highest and lowest spectral frequencies, the noise on each ratio increases as one moves away from the center of the frequency range.

To determine whether the observed modes were saturated, thin (68 mg) samples ($\approx$ 1/4 of the optical thickness of the larger samples) were measured. In the coarse grind thin sample, the 7.7 cm^{-1} mode was too weak to observe. The integrated line strength of the 8.3 cm^{-1} mode was 0.3 ± 0.1 times as intense as in the thicker sample. In the fine grind thin sample the integrated line strength of the 8.3 cm^{-1} mode was

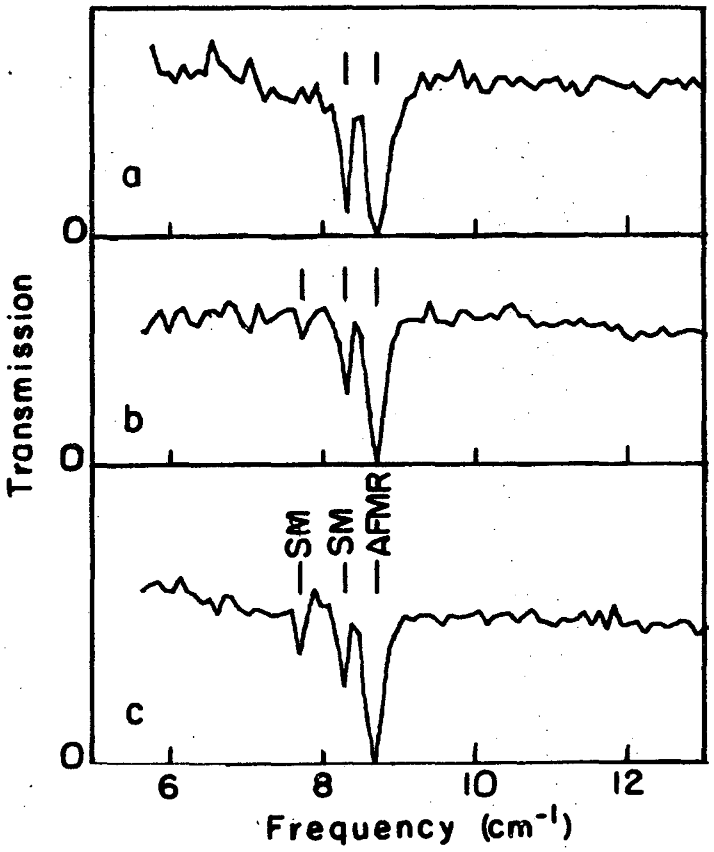

XBL738-1610

Fig. 7. Transmission spectra of MnF_2 powders. (a) fine grind (0.06 cm^{-1} resolution); (b) intermediate grind (0.08 cm^{-1} resolution); (c) coarse grind (0.08 cm^{-1} resolution). SM indicates possible surface magnon mode.

0.50 ± 0.05 times its intensity in the thicker fine grind sample. The integrated absorption strength of a mode varies linearly with optical thickness for a non-saturated mode with a Lorentzian lineshape and as the square root of the optical thickness for a saturated mode. Saturated and non-saturated modes with Gaussian lineshapes vary as $\sqrt{\log}$ and log of the optical thickness. The results from the thin samples indicate, therefore, that the 8.3 cm^{-1} mode is saturated in both thick and thin fine grind samples. In the coarse grind samples, however, the mode is saturated only in the thicker sample. Because the mode is just barely saturated in the thicker coarse grind sample, we can estimate from the integrated absorption strength a linewidth of order 0.05 cm^{-1}.

Figure 8 shows a logarithmic plot of integrated absorption strength vs surface-to-volume ratio (SVR). A reasonable fit for the 8.3 cm^{-1} mode is obtained to a $\sqrt{\mathrm{SVR}}$ dependence as is expected for a saturated surface magnon mode. If we assume that the coarser grind samples had a higher correlation among their axes than the finest grind (due to screening both above and below), the data for the coarser samples are brough closer to the $\sqrt{\mathrm{SVR}}$ line.

The strength of the 7.7 cm^{-1} mode has a more complicated dependence on surface area than the 8.3 cm^{-1} mode. If this is a surface magnon, it may possibly be associated with a non-cleavage plane while the 8.3 cm^{-1} mode is associated with a cleavage plane. However, there is no good explanation as yet for the behavior of this mode.

The magnet cryostat described earlier has been used to measure the magnetic field dependence of the finest grind powder spectrum. When a magnetic field is applied to MnF_2, as discussed earlier, the AFMR splits linearly if the field is parallel to the c axes and quadratically if the

Fig. 8. Logarithmic plot of integrated absorption strength vs surface-to-volume ratio. Shaded rectangles refer to 8.3 cm^{-1} mode, unshaded to the 7.7 cm^{-1} mode. The rectangle "a" represents a single crystal of approximately the same volume as the powder samples. (The surface area of this crystal was measured directly to within 10%.) The width of each rectangle indicates the uncertainty in our measurement of the SVR given in Table C. The height of the rectangle indicates error in intensity measurement due to bolometer noise. The 8.3 cm^{-1} mode intensity shows less error since it was measured from a ratio of a zero field spectrum to a 45 KG field spectrum of the same sample. This method of measuring mode intensity gave considerably lower error due to noise.

Neither of the two modes appears in the single crystal, and the 7.7 cm^{-1} mode does not appear in the finest grind sample. The heights of the rectangles in these cases merely reflect the noise level on the spectrum. The straight line shows the $\sqrt{\mathrm{SVR}}$ dependence expected for a saturated Lorentzian surface mode.

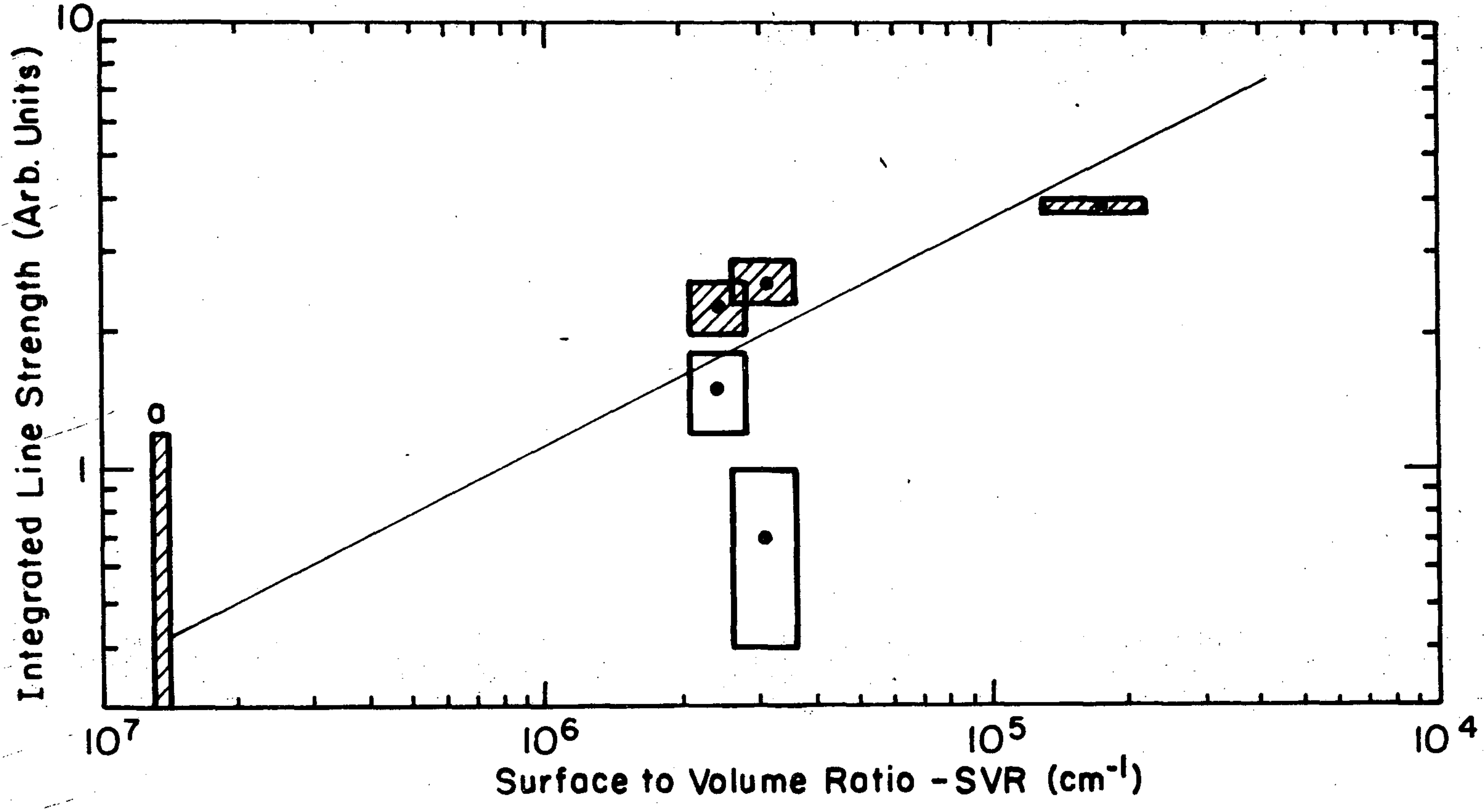

XBL744-6186

Fig. 8

field is perpendicular to the c axis. When the field is applied to powdered MnF_2, the splitting should vary from linear to quadratic, depending on the orientation of each crystallite. The result is a broadened absorption with a sharp edge on the low and high frequency sides. The crystallites which absorb at this edge are those whose c axis is parallel to the applied field and whose AFMR splits linearly. By measuring the position of this edge, we may determine the g factor of the splitting. According to the theory of surface magnons, the magnetic field dependence of the surface mode should be the same as that for the AFMR, assuming that the surface spins in equilibrium lie along the c axis, Consequently, we should see a smaller absorption edge from the surface mode lying below the AFMR absorption edge by an amount equal to the separation between the surface mode and the AFMR.

Figure 9 shows the ratio of fine grind powder spectra taken at various magnetic field strengths to spectra taken in zero field.

Figure 10 shows a plot of frequency vs field obtained from these data. The observed g factors are 2.06 ± 0.08 for the AFMR and 2.00 ± 0.15 for the 8.3 cm^{-1} mode. It is interesting to note in Fig. 9 that the edge of the 8.3 cm^{-1} mode is somewhat broader than that of the AFMR. This suggests that there might be a range of g factors associated with this mode.

We see from Fig. 9 that by applying a magnetic field, we may spread out both resonances to the point where, near the absorption edges, the modes are no longer saturated. Computing the absorption coefficient from the ratio spectrum at 10.44 KG, we obtain Fig. 11. Under the assumption that the 8.3 cm^{-1} mode splits in the same manner as the bulk

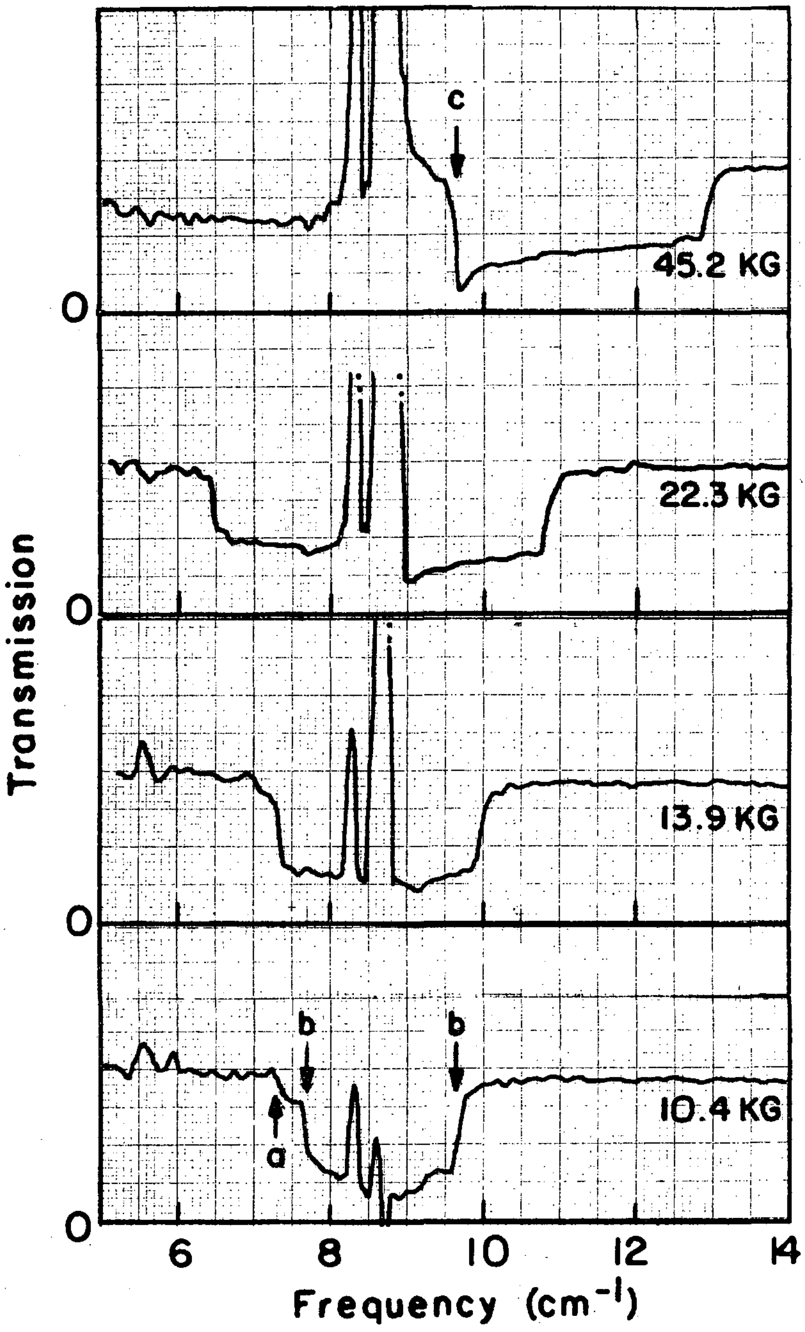

XBL738-1612

Fig. 9. Ratio of spectra of fine grind sample (field on/field off) for various field strengths. a = 8.3 cm^{-1} mode absorption edge due to linear splitting; b = AFMR linear splitting edge; c = AFMR quadratic splitting edge.

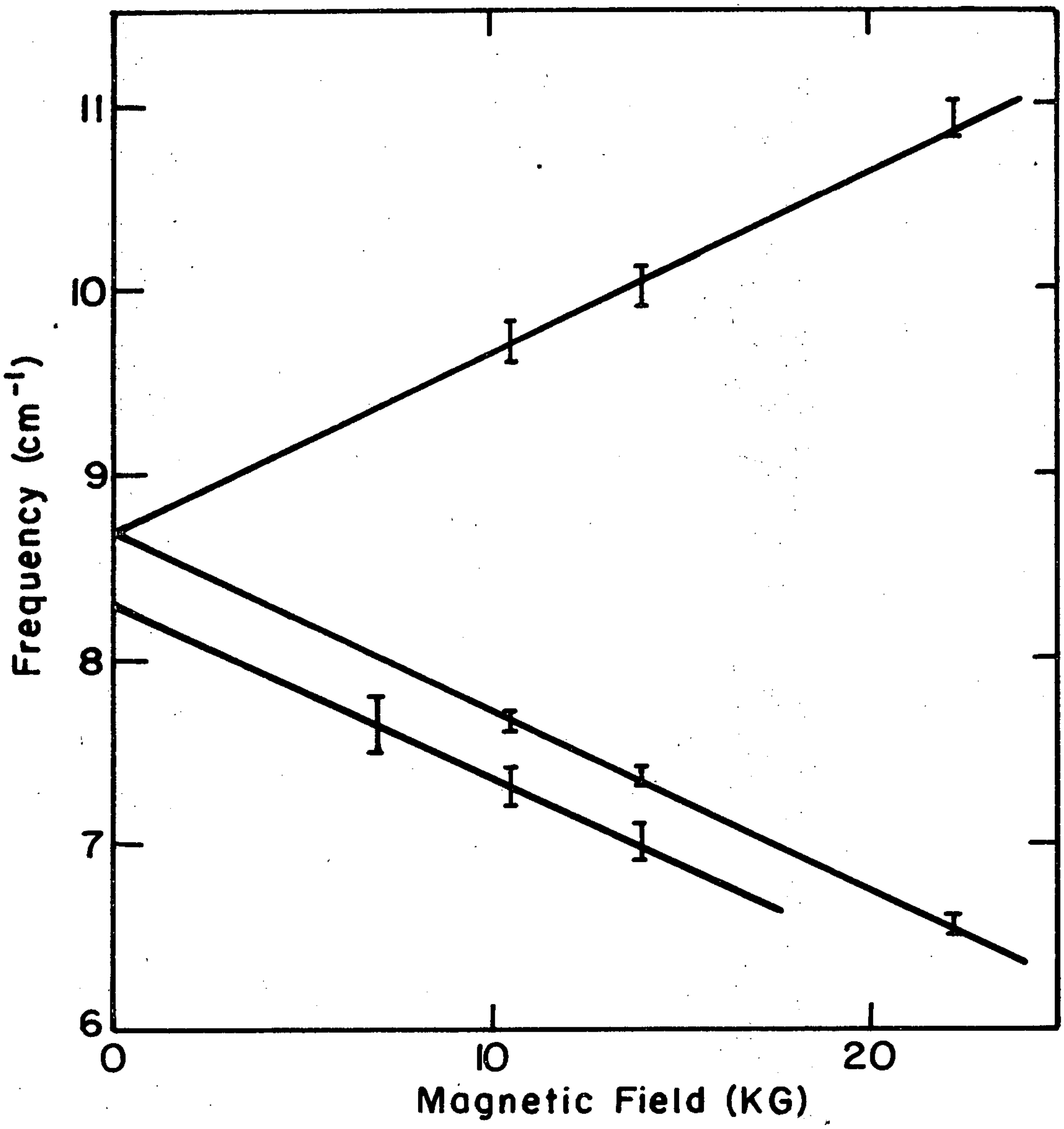

XBL 738-1613

Fig. 10. Magnetic field dependence of AFMR and 8.3 cm^{-1} mode absorption edges. Only the $H_{\|}$ absorption edges (a and b of Fig. 9) are shown.

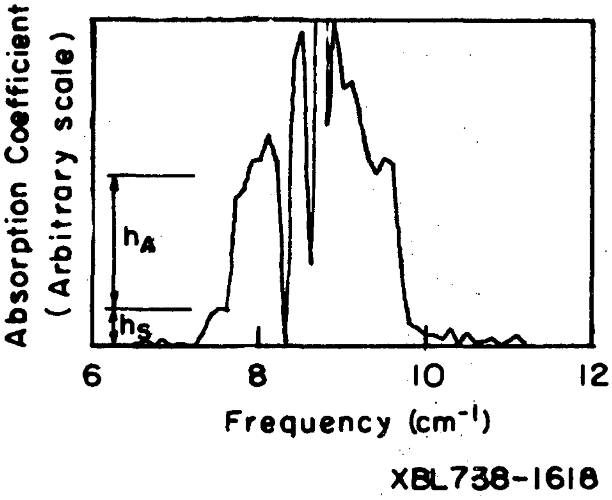

Fig. 11. Absorption coefficient from MnF_2 fine grind powder ratio (10.44 KG/0 KG). h_S = height of 8.3 cm^{-1} mode absorption edge. h_A = height of AFMR absorption edge.

resonance in all crystallites, we can obtain the relative intensities of the two modes from a ratio of the heights of the absorption edges in Fig. 11. The 8.3 cm^{-1} mode intensity is observed to be about 25% of the AFMR intensity. This implies that the saturated zero field intensity ratio would be 50% which is about what is measured from Fig. 7a.

Having considered the positive evidence for identifying the 8.3 cm^{-1} mode as a surface magnon, we should consider whether there are other possible ways to explain the observed data. There are several possibilities which suggest themselves, but all for one reason or another may be discounted.

We may be sure that the mode is not an edge or vertex resonance since the absorption strength of these would vary as SVR and $SVR^{3/2}$ respectively for a saturated mode. The dependence on SVR also eliminates impurities as a source of the mode since the strength of an impurity mode should be independent of particle size. Contamination of the samples in preparation may be eliminated since similarly prepared samples of MnF_2 doped with a few percent of Co, Fe, and ZN do not show this mode. (We shall discuss impurity doping in Section III of this thesis.)

The possibility of demagnetization effects causing the observed resonances is eliminated for two reasons. First, from Table 1 and Eq. (12) demagnetization modes all lie above the AFMR within 0.13 cm^{-1}, which is too near the AFMR and in the wrong direction to account for the observed modes. Second, demagnetization modes depend strongly on sample shape, and we would expect any mode split off from the AFMR by shape effects to be broadened on the order of the splitting by the randomness of the particle shapes. This disagrees with the observed sharpness of the powder modes.

A related possibility is that the interaction of demagnetizing fields in a closely packed powder might cause resonance changes similar to those which occur in dielectric powders.[45] This possibility could be eliminated by the same arguments which apply to the magnetostatic hypothesis. However, to be sure that we were not overlooking something, we took a spectrum of the dilute sample previously described. This spectrum showed the 8.3 cm^{-1} mode as strongly as the non-dilute case. We did not see, nor did we expect to see, the 7.7 cm^{-1} mode in this fine grind sample.

Interaction of the powders with the parawax may be eliminated as a source for the 8.3 cm^{-1} mode because the spectrum of the coarse grind powder sample which was not saturated with paraffin showed the 8.3 cm^{-1} mode as strongly as that of the saturated sample. No 7.7 cm^{-1} mode was observed in this sample, however. It is unlikely that the 7.7 cm^{-1} mode was missing because of the absence of a surrounding dielectric since interaction between the dielectric and the powder should occur much closer to a resonance than the 7.7 cm^{-1} mode is found. It is possible that the absence of paraffin from the surface of the particles meant that the surface magnetic parameters were different; although, if this were the case, the 8.3 cm^{-1} mode should have been strongly affected as well.

One other possible explanation for the modes was strains introduced by grinding. The likelihood of this explanation does not seem great because of the annealed sample results which showed both the 7.7 cm^{-1} and the 8.3 cm^{-1} modes. The 8.3 cm^{-1} mode intensity relative to the AFMR was equal to the value expected assuming annealing had no effect.

However, the above mentioned peculiarities of color and weight observed in the annealed sample suggest that, for some reason, the sample may not have veen satisfactory for testing the strain hypothesis.

B. Microwave Experiment

To ascertain whether the observed powder modes are actually surface magnons, an attempt was made to observe these absorptions in single crystal samples with 150 GHz microwaves using the second harmonic generator, the klystron, and the magnet cryostat described above. There is some evidence that the 8.3 cm^{-1} mode was seen by Johnson and Nethercott in their original microwave work on the MnF_2 AFMR. They observed a resonance 3000-4000 gauss below the AFMR.[1] This corresponds roughly to a mode at 8.4 - 8.3 cm^{-1}. They also observed a number of other modes below the AFMR frequency, but none so far below as this one. None of these modes were identified as to origin and some may have been demagnetizing modes.

Three different types of samples were used for our microwave experiments. The first sample was 273 mg of the fine grind powder which was tamped into a short section of waveguide immersed in parawax, and hung in the magnet core at the end of the flanged waveguide cryostat insert described previously. Figure 12 shows the measured transmission as a function of field. The g value obtained for the AFMR is 2.06 ± 0.01. The exact shoulder on the possible SAFMR is hard to determine because it is so broad. However, if we assume that the small kink in this shoulder represents the typical g factor of this mode, the result obtained for the mode is $g = 2.01 \pm 0.02$. Both g values are in good agreement with those obtained from the far infrared data.

It is interesting to note that it was necessary to immerse the

0 0 0 0 3 9 0 0 8 4 5

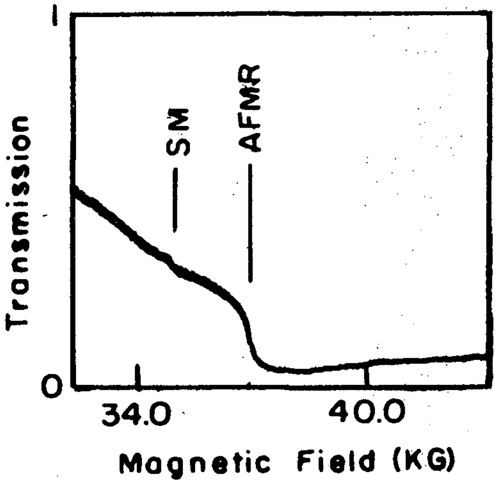

XBL738-1619

Fig. 12. Fine grind powder microwave experiment. The AFMR and possible surface mode absorption edges are shown. The surface mode edge is quite broad and its exact position is uncertain so the small "kink" in the curve is taken to be the characteristic value.

powder in parawax in order to get reproducible results. Presumably, this is because the anisotropic magnetic susceptibility caused the powders to rotate in a strong applied magnetic field.

Many microwave runs showed spontaneous jumps of 5-10% in absorption. These did not occur reproducibly, and, although they remained unidentified, were assumed to be instrumental in nature perhaps due to some change in the harmonic generator's characteristics.

The remaining two microwave samples were single crystals. The first consisted of an approximately rectangular slab a few mils thick from the pink Catalano material. This slab was about .6 cm long and .15 cm wide. The sample was oriented with the long axis parallel to the c axis and the largest surfaces in the (110) cleavage plane. The sample was shaped first by cleaving, then by sanding down to the desired thickness with #600 grit paper. For ease of orientation in the waveguide, the sample was also cleaved or sanded along a plane perpendicular to the 110 face and parallel to the c axes. The sample was held in a straight section of waveguide with its c axis parallel to the guide, by a bent sliver of polyethylene. The waveguide section was attached to the waveguide cryostat insert, as in the case of the powder.

It was necessary to grind the sample quite thin to reduce the large number of Fabry-Perot interference resonances observed in thicker samples. These resonances occur when the increasing index of refraction of a material near a resonance causes the wavelength of microwaves in the sample to be shorter than the sample dimensions. Resonances occur when some length of the sample corresponds to a half-integral number of wavelengths. This effect seems to be much reduced, although still present, when the sample is ground to ≈ 5 mils.

Figure 13 shows the results of the 110 face crystal run.

Assuming the AFMR and Fabry-Perot fringe identification is correct, no surface resonance was seen in this sample. If the 8.3 cm^{-1} mode were associated with this surface, it would appear about 1A below the AFMR. Its intensity, taken from the infrared data and scaled according to surface-to-volume ratio, should be $\gtrsim$ 1/40 of the AFMR intensity. Therefore, if the 8.3 cm^{-1} mode were as broad as the AFMR appears to be, it might not be seen above the noise level. It could also be that this mode is not associated with the 110 surface, and that modes associated with the 110 surface lie too close to the AFMR to be distinguished from it.

Some support is given to this last supposition by our third sample. This sample was a similarly sized crystal (thickness ≈ 5 mils) whose largest surface was ground in the 111 direction. The crystal was oriented by X-rays, cut with a diamond saw, and ground like the others to the desired shape. It was necessary to use a specially shaped piece of waveguide to hold this sample with its c axis properly aligned in the applied magnetic field. This waveguide has been described earlier. Because of the 46° tilt of this piece of waveguide, it was possible to place the sample in the guide either with the c axes about parallel to the applied field, or with it about perpendicular to the applied field. Figure 14 shows the results of this run.

Unfortunately, these experiments were done rather hurriedly and the sample used was not marked as to c axis orientation. Therefore, it is not known which orientation corresponds to which results. Another problem with the run is that the AFMR did not appear in either orientation,

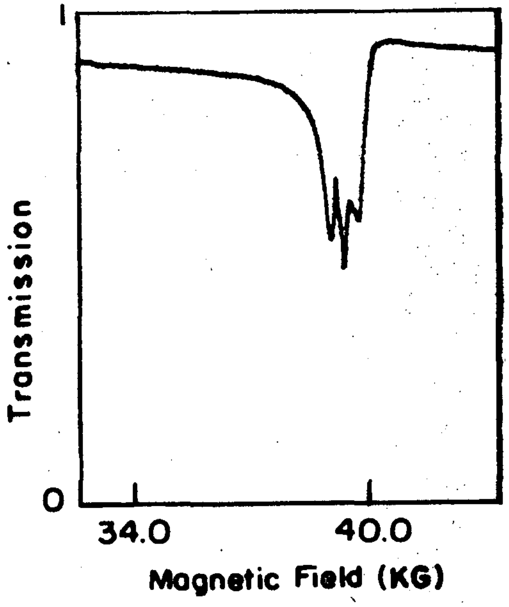

XBL738-1620

Fig. 13. Microwave transmission experiment- (110) surface. The AFMR is displaced upward in field strength from the powder value, presumably because the sample was not well aligned with the field. The multiple peaks at the resonance are most likely Fabry-Perot interferences.

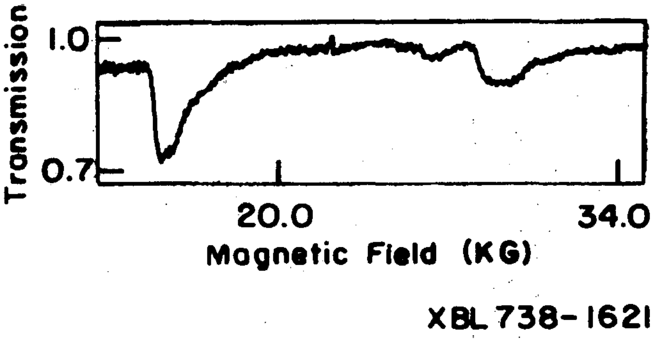

Fig. 14. Microwave transmission experiment-(111) surface. One of the two possible orientations showed the two resonances observed above. Neither showed the antiferromagnetic resonance. Using a g-factor of 2 and assuming the resonance at zero field lies above the microwave frequency, the higher field resonance has a zero field value of 7.7 cm^{-1}, and may correspond to the lower observed infrared resonance.

possibly because the crystal was canted when placed into the waveguide, and the magnetic field could not split the mode enough to be observed. If we assume a g factor of 2, that the c axis is aligned with the field, and that the zero field modes lie above the microwave frequency, the zero field frequencies are 6.4 cm^{-1} and 7.7 cm^{-1}. Because the AFMR does not appear, we can not be completely sure of our alignment and thus also of our frequency assignments.

These results for the 111 face suggest that the 8.3 cm^{-1} mode might be found on the 011 cleavage plane. This cleavage plane is more like the 111 face magnetically than like the 110 face because on the 011 face the c axis is not parallel to the face but rather forms a 34° angle to the plane. An investigation of this surface is definitely needed.

C. Analysis

1. Theory of SAFMR

A surface antiferromagnetic resonance (SAFMR or surface magnon) is a spin wave mode similar to the bulk AFMR mode but having only a finite penetration depth from the surface into the crystal. This mode arises from the difference between the magnetic environment of the surface ions and that of the bulk ions. Thus the SAFMR is to be distinguished from demagnetization modes discussed earlier which arise from gross sample shape effects. In the surface layer (or layers, for some crystal planes), the ions see only a fraction of the exchange energy seen by bulk ions because one or more of the antiferromagnetic neighbors has been removed. The direction of the exchange field may also be shifted from the c axis by the asymmetry introduced by the surface. Similarly the anisotropy field may be shifted in direction and changed in magnitude by this absence of neighboring ions. If the cleavage plane of a crystal has a surface mode, we might expect this mode to appear as a sharp absorption in powder spectra because of the predominance of cleavage planes on the particle surfaces.

As mentioned earlier, the easiest way to treat surface modes theoretically is to use the linear chain model. For a surface mode we need a semi-infinite linear chain with different exchange and anisotropy fields in the surface layer.

We may use the infinite set of Eqs. (7), except that we must add equations for the surface layer:

$$\omega\, S^{+}(a,o) = -\,\mu(H_A' + \frac{3}{4} H_E')\, S^{+}(a,o) - \mu \frac{H_E'}{2} S^{+}(b,o)$$

$$- \mu \frac{H_E'}{4}\, S^{+}(b,1),$$

$$\omega\, S^{+}(b,o) = \quad \mu\, (H_A' + \frac{3}{4} H_E')\, S^{+}(b,o) + \mu \frac{H_E'}{2} S^{+}(a,o)$$

$$+ \mu \frac{H_E'}{4} S^{+}(a,1). \qquad (35)$$

Here we have explicitly taken into account the reduced number of neighbors of the surface ions. Changes in H_E and H_A due to asymmetry and possible surface distortion of the position of surface ions are indicated by the prime notation. To reduce the system of equations to a finite number, a decaying exponential form of the spin wave is assumed. The decay lengths may be found as a function of the SAFMR frequency from the bulk equation (8). Solving this equation yields two decay lengths, the full solution being a sum of two decaying exponentials.

The SAFMR frequency is found by solving the secular equation derived from Eqs. (35) and (7) in the decaying exponential approximation. This secular equation for the 011 or 110 surface is

$$\begin{vmatrix} \mu\,(H_A' + \frac{3}{4} H_E')+\omega & \mu\,\frac{H_E'}{2} & 0 & \mu\,\frac{H_E'}{4} & 0 & 0 \\ \mu\,\frac{H_E'}{2} & \mu\,(H_A' + \frac{3}{4} H_E') - \omega & \frac{\mu H_E'}{4} & 0 & 0 & 0 \\ 0 & \mu\,\frac{H_E'}{4} & \mu\,(H_A + H_E) + \omega & \mu\,\frac{H_E}{2} & 0 & \mu\,\frac{H_E}{4} \\ \mu\,\frac{H_E'}{4} & 0 & \mu\,\frac{H_E}{2} & \mu\,(H_A + H_E) - \omega & \mu\,\frac{H_E}{4} & 0 \\ 0 & 0 & 0 & \mu\,\frac{H_E}{4}\,(1+e^{-\lambda}) & \mu\,(H_A + H_E) + \omega & \mu\,\frac{H_E}{2} \\ 0 & 0 & \mu\,\frac{H_S}{4}\,(1+e^{-\lambda}) & 0 & \mu\,\frac{H_E}{2} & \mu\,H_A + H_E - \omega \end{vmatrix} = 0 \qquad (36)$$

where λ is either of the two decay lengths.

Dr. T. Wolfram of the Rockwell International Science Center has solved this equation using standard matrix inversion techniques on a computer.

His solution takes as inputs the crystal surface, the bulk crystal exchange and anisotropy parameters, and the observed resonance frequency attributed to the possible surface mode. It predicts mode decay lengths, λ, and a range of surface exchange and anisotropy parameters, H_E' and H_A'. Figure 15 shows the range of exchange and anisotropy for the (110) and (011) crystal planes, as well as anisotropy ratios for the (111) plane.

It is clear that some fairly drastic changes in anisotropy and exchange energy must take place at the surface to account for the observed modes. Changes in surface magnetic environment are not easily measured directly, and thus this part of the theory has not been verified by experiment.

The decay length of the mode, however, is subject to more direct investigation. If the spin wave amplitude in the SAFMR is similar in magnitude to that in the AFMR, then we would expect the ratio of the intensities of the two modes $\frac{I_S}{I_A}$ to be proportional to the volume of sample occupied by the moving spins in each mode. Thus

$$\frac{I_S}{I_A} = (\mathrm{SVR})\ \lambda \qquad (37)$$

where λ is the decay length of the mode. Wolfram's results for the 110 or 011 face show that one decay length is considerably longer than the other. This longer decay length is 12 lattice spacings in the 011 or 110 direction. This is a distance of about 70 Å in MnF_2. Thus, for the finest grind

Eq. (37) gives $I_S/I_A = 1785 \times 7 \times 10^{-7} = 1.2 \times 10^{-3}$, or about 200 times smaller than the observed ratio of 0.25. A computation of λ from the observed mode intensity ratio and Eq. (37) gives a value of 1.5μ for the experimental decay length.

2. Enhancement of the Surface Mode and Surface Ferromagnetism

This anomalously large surface mode intensity is not without precedent. Heat capacity measurements in polycrystalline YIG samples by Henderson, *et al.*[46] have shown a linear term which was tentatively attributed to ferromagnetic surface spin waves, but which was 30 times too large.

Enhancement effects of several thousand times have been observed in other magnetic resonance phenomena. Gossard and Portis have observed enhancement of nuclear magnetic resonance in Co powders due to the motion of ferromagnetic domain walls.[47] The Gossard-Portis effect occurs when an RF field is applied to a ferromagnetic particle which is so small that it can have only a few antiparallel domains. If the direction of the applied field is parallel to the domain magnetization, the size of the parallel domains will increase at the expense of the antiparallel domains. If the domain structure is weakly bound, the motion of the domain walls will be large. The nuclei in the region of the particle through which the domain wall moves will see an oscillating field equal in amplitude to the magnetization of the sample. This magnetization field is on the order of hundreds of gauss and thus many orders of magnitude greater than the applied RF field. The strength of the nuclear resonance is correspondingly increased.

It seems possible that ferromagnetic effects induced by the asymmetry of the crystal at the surface might cause the apparent enhancement of

Fig. 15. Variations in surface exchange and anisotropy required to match the frequencies of the two extra modes observed in the far IR. ——— refers to 8.3 cm^{-1} mode, --- refers to 7.7 cm^{-1} mode. The value of the bulk anisotropy used in these calculations was $0.01625H_E$ in agreement with the numbers given by Kotthaus and Jaccarino.[9] A more accurate value is $0.015H_E$ taken from the neutron data in Table 1; however, the difference is insignificant for our purposes.

The use of these graphs may be illustrated as follows: From the graph for the (011) face we see that if the exchange field at the surface <u>per next nearest neighbor ion</u> ($1/8\ H_E'$) is the same as the bulk exchange <u>per next nearest neighbor ion</u> ($1/8\ H_E$), the surface anisotropy will be only $0.0025\ H_E$ or 2/15 of the bulk anisotropy for the 8.3 cm^{-1} mode. For the 7.7 cm^{-1} mode the surface anisotropy will be negative unless the per ion surface exchange energy is less than 1/2 of the bulk exchange.

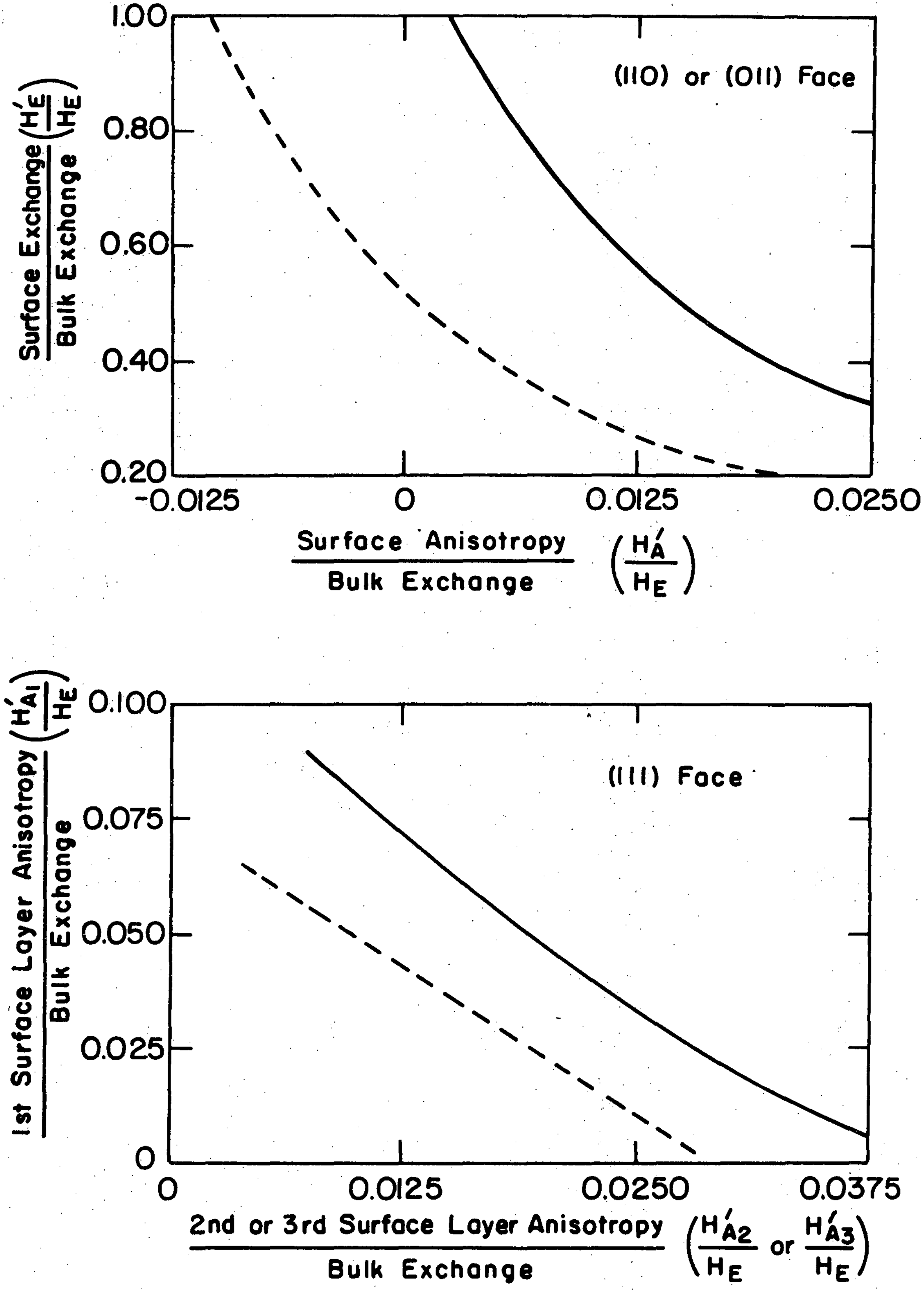

XBL 738-1622

Fig. 15

the surface magnon resonance. Professor W. Wolf at Yale several years ago noticed a small anomalous ferromagnetic component in the magnetic susceptibility of an antiferromagnetic powder. This ferromagnetism appeared at the Neél temperature and was about 10^{-4} times the bulk susceptibility.[48]

Wolfram's theory shows that a considerable change in the magnitude of the exchange and anisotropy parameters must occur in the surface layers to account for the observed mode frequencies. It seems possible that the anisotropy and exchange fields change direction in the surface layers due to distortions in atomic position and lack of symmetry. Dr. T. Holden of the Chalk River Nuclear Laboratory has described an experiment with polarized neutrons on Zn-doped MnF_2 which showed that the Mn spins cant away from the c axis in the presence of Zn ions.[47] Magnetically Zn atoms act like vacancies, and it seems likely that the entire half-space of vacancies seen by surface Mn ions would cause the surface ions to cant as well.

To have true ferromagnetism it is necessary to have more than just a net surface magnetic dipole moment. Neighboring spins on opposite sublattices must prefer to tilt in the same direction, and the net magnetic moment formed must not be rigidly fixed in direction with respect to the surface. If these conditions are supposed to exist, however, only a very small canting is required to obtain a factor of 200 enhancement of the local applied fields to account for the observed surface magnon strength.

Mr. D. Woody[50] suggested an experiment which could test in part whether the large surface mode strength was due to a long penetration depth, or to some enhancement effect. If the mode were due to a long penetration depth, then in a very fine grind powder (grains ≈ 2 μ dia.) the mode would rob essentially all of the bulk AFMR strength because the penetration depth would be on the order of the particle size. Such a sample should certainly be tested.

CHAPTER III. ALLOY STUDIES

A. Background

1. Introduction

Using the experimental techniques already described, we have measured far infrared powder transmission spectra of the alloy systems (Co,Mn)F_2, (Fe,Mn)F_2, and (Zn,Mn)F_2. Our results complement the experimental work using neutrons, Raman, and far-IR (two-magnon) spectroscopy by groups at Oxford, Chalk River, and elsewhere.[15-22] The far-IR techniques are ideally suited for studying the effects of alloying on those resonant modes which show the greatest effects of long range order, namely the zone center modes. The results we have obtained show some previously unexpected effects which may be given a simple theoretical motivation. Our results also provide a basis for partially checking the extensive theoretical work done on these systems, in particular the applications of the Coherent Potential Approximation.[51-54] Our work divides naturally into two parts: the magnetic-magnetic alloys (Co,Mn)F_2 and (Fe,Mn)F_2, and the non-magnetic-magnetic alloys (Zn,Mn)F_2. After a brief theoretical introduction and review of experimental techniques used, we shall discuss the results for each type of system separately.

2. Theory

The Heisenberg Hamiltonian of Eq. (1), where the spin, anisotropy, and exchange vary from site to site, is the starting point for alloy theories. The most powerful method for determining resonance frequencies and linewidths of magnetic modes is an adaption of the Coherent Potential Approximation (CPA) by Buyers, Elliott, and Pepper[51,52] to antiferromagnetic systems. The CPA is a self-consistent Green's function method which starts with the Heisenberg Hamiltonian of the alloy and develops an effective pure material Hamiltonian with the same eigenvalues as the alloy Hamiltonian. One of the most important properties of the CPA is that it treats the concentrated impurity region where more straightforward theories become too complex to use.

Green's functions have also been used in the dilute case apart from the CPA.[22] However, a simpler approach can also be used for dilute materials. In the case of a single impurity (say Mn^{++} in a host lattice such as FeF_2), one may sometimes obtain good agreement with data by considering the motion of only a cluster of host ions around the defect and treating the remaining host ions as rigidly fixed with antiparallel spins . For a cluster of ions which includes only the next nearest neighbors of the defect, we have the following hamiltonian:

$$\mathcal{H} = -S_Z'(0)(H_A' - 2I_{eNN}S \sum_{i=1}^{8} I_{eNNN}S_Z(i)) - \sum_{i=1}^{8} S_Z(i)(H_A - 2I_{HNN}\, S + 7I_{HNNN}S)$$
$$+ 1/2\; Je_{NNN} \sum_{i=1}^{8} [S'^{+}(0)\, S^{+}(i) + S'^{-}(0)\, S^{-}(i)], \qquad (38)$$

where S' and H_A' refer to the defect parameters, Ie is the geometric mean between host-host exchange (I_H) and defect-defect exchange (I_D) and NN and NNN refer to nearest neighbor and next nearest neighbor respectively.

A further step towards simplicity is the Ising or spin-flip model. This is essentially a cluster model with only one ion in the cluster. In this model the defect spins considered may occupy only certain quantum states each separated by the frequency:

$$\omega_D = H_A' - 2I_{eNN}S + 8\ I_{eNNN}\ S. \qquad (39)$$

A pair of next nearest neighbor defects in this model would have the frequency:

$$\omega_p = H_A' - 2\ I_{enn}\ S + 7\ I_{eNNN}\ S + I_D\ S', \qquad (40)$$

and so on for higher order defect groupings.

The principal shortcoming with the cluster and Ising approaches is that they should apply primarily to short wavelength resonances on the order of the cluster size and hence be of little value in the long wavelength AFMR region of our experiments. Indeed, Buchannan, et al.[20] have found that the Ising model works quite well (about as well as the CPA) in explaining Raman data for the two magnon resonance, even at high impurity concentrations.

One of the interesting results of our experimental work is that the Ising model also gives a good estimate of the resonance frequency of defect modes split off of the host material AFMR.

3. Experimental Notes

Polycrystalline samples were grown from the melt using nominally pure ZnF_2, CoF_2, MnF_2, and FeF_2. The samples were then ground to powder with average grain size < 100 μ. Samples weighing either 28 or 276 mg were then formed into the brass sample holder described earlier and saturated with paraffin.

Far-infrared spectra of these samples were measured at LHe temperatures over the frequency range 5-100 cm^{-1} by Fourier transform spectroscopy using the techniques and instrumentation also described previously. The spectral resolution varied from 0.2 to 0.7 cm^{-1} and was selected to resolve all features seen. The spectra were ratioed against similarly prepared samples of ZnF_2 so as to remove the effects of phonon absorption and powder scattering.

B. Results for Magnetic-Magnetic Systems

The frequencies of the observed modes in $(Co,Mn)F_2$ are shown as a function of concentration in Fig. 16. (Points in the figure indicate absorption peaks, while flags indicate the approximate widths of the resonances.) Figure 17 shows typical spectra of this system. In nearly pure CoF_2 the 37 cm^{-1} mode is identified as the CoF_2 AFMR. As the impurity level is increased this mode shifts rapidly upwards in frequency in the direction of the 124 cm^{-1} mode of isolated Co ions in MnF_2.[18] It also broadens asymmetrically towards higher frequencies. Scattering at frequencies above 100 cm^{-1} in the powder samples used prevented measurements of the behavior of this mode at high Mn concentrations.

The 28.5 cm^{-1} mode is relatively narrow and weak in the nearly pure CoF_2 samples. The mode intensity increases linearly with concentration up to about 1% impurity and after that increases much more slowly. This mode may be identified with the 30 cm^{-1} defect mode predicted by Cowley and Buyers[22] from their Green's function calculations. The defect mode drops in frequency with increasing Mn concentration to become the 8.7 cm^{-1} (AFMR) mode in pure MnF_2.[1]

The third mode at 32 cm^{-1} (0.96 THz) which appears in CoF_2 doped with 0.3%-10% MnF_2 is most reasonably ascribed to pairs of Mn impurities

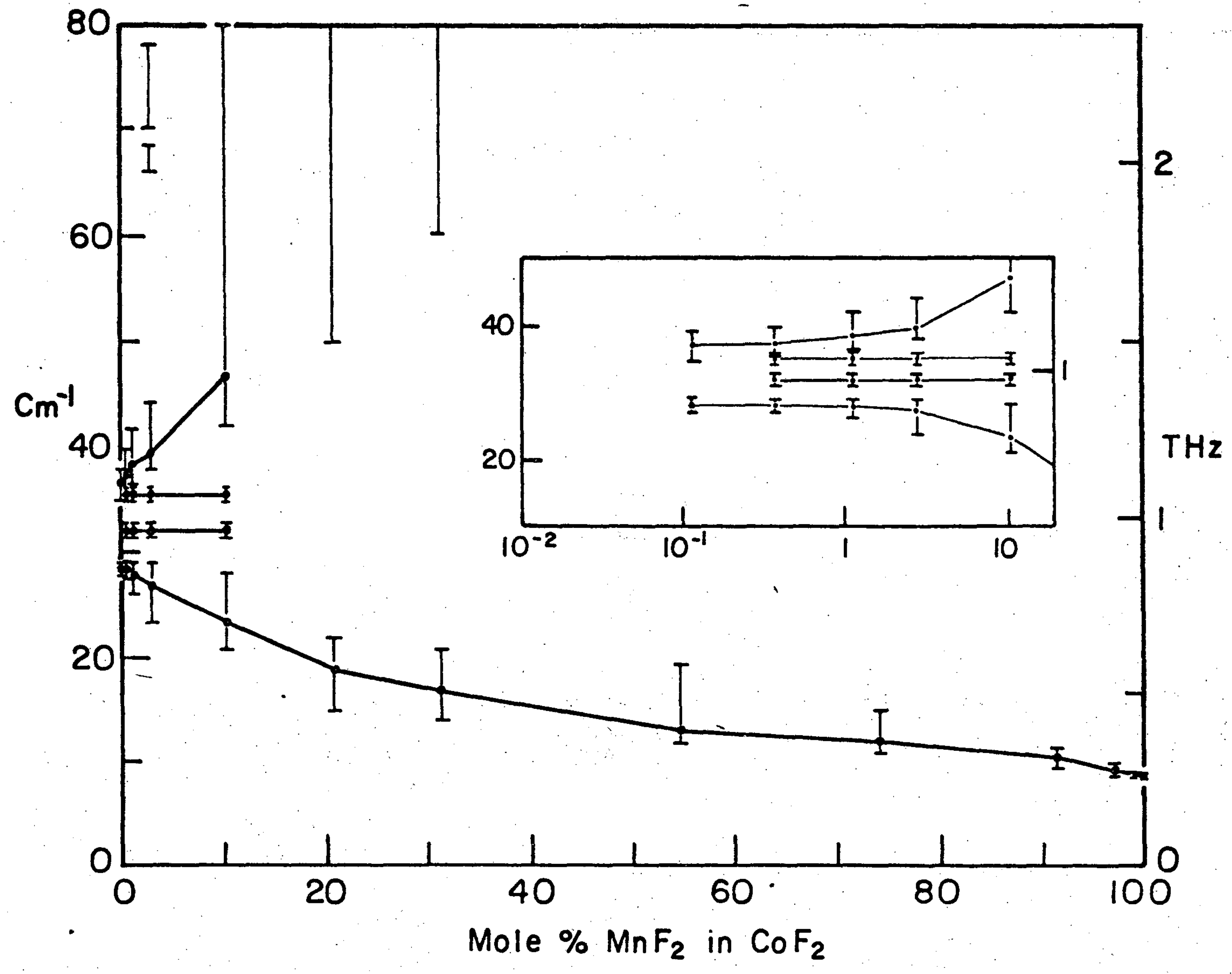

XBL 7210-7118A

Fig. 16. Center frequencies and widths of far-infrared absorption lines in (Co,Mn)F$_2$.

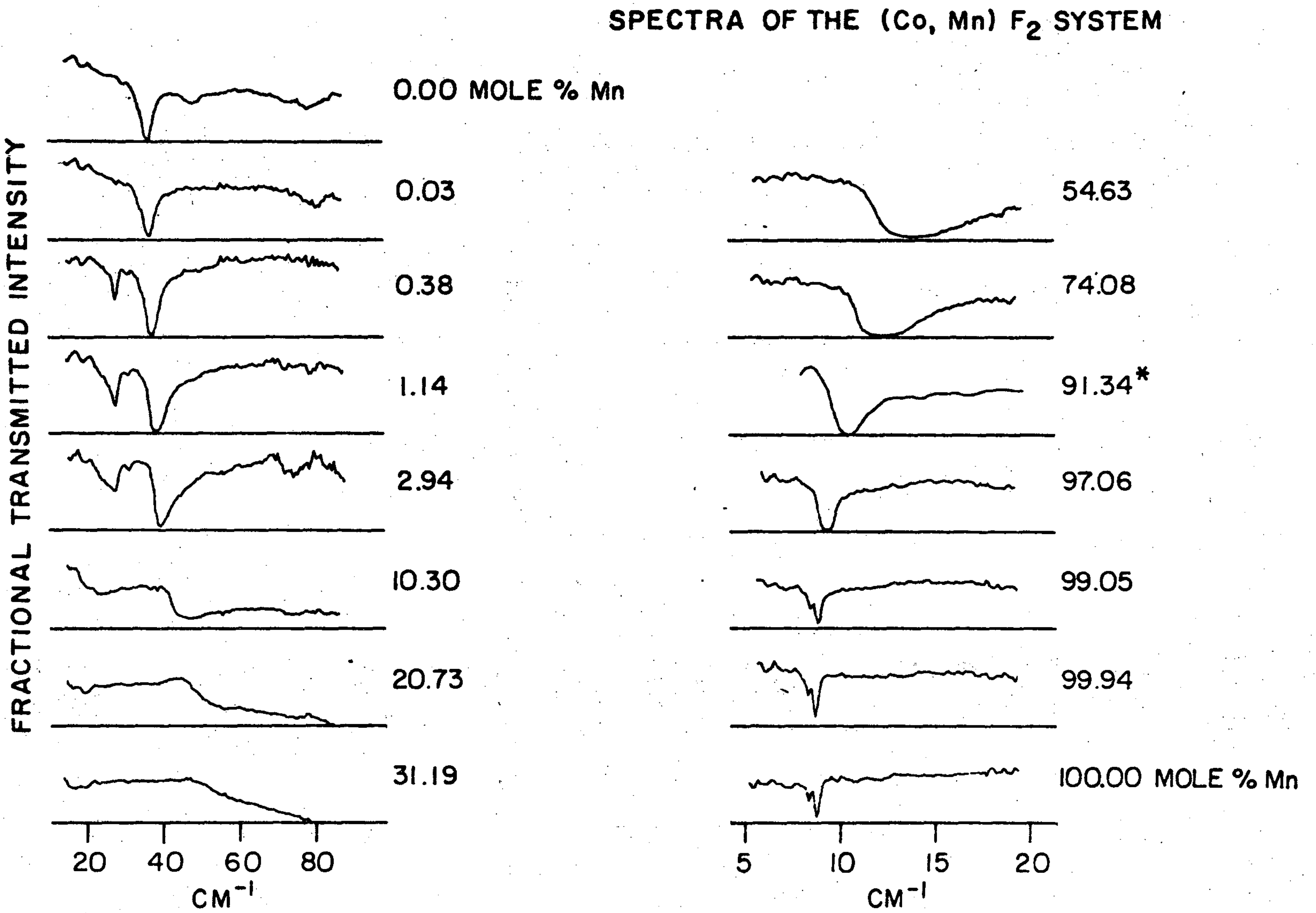

XBL7211-7223

Fig. 17. Spectra from which some of the data in Fig. 16 were taken. Note the SAFMR appearing in the nearly pure MnF_2 samples.

on opposite sublattices. Its position may be roughly calculated from an Ising approximation. Assuming that the 28.5 cm^{-1} mode is a defect mode, each next nearest neighbor contributes ≈ 1/8 of the energy. Therefore, if we add 7/8 of the lower mode energy (24.9 cm^{-1}) to the 6.2 cm^{-1} Mn-Mn exchange energy, we obtain 31.3 cm^{-1}, which is very close to the observed value. Further evidences for this assignment are: (1) there is no change of frequency or linewidth with concentration; (2) the resonance appears at relatively high impurity concentrations compared with the defect mode, and then disappears as the concentration increases further. Such a mode would necessarily be localized.

Another mode at 35.5 cm^{-1} appears in the 0.38% to 10% samples and is probably due to a Mn defect site with two Mn next nearest neighbors. This triplet mode is twice as far from the defect mode as is the pair mode and has about one-fourth the pair mode intensity.

Cowley and Buyers also predict five localized modes between 71 cm^{-1} and 76 cm^{-1}. These modes are associated with the host neighbors of the defect ion. Weak absorptions have been observed at 67.0 ± .5, 70.5 ± .5, 72.5 ± .5, and 75.0 ± .5 cm^{-1} in single crystal specimens of CoF_2 with $\lesssim$ 0.03 percent Mn. These neighbor modes can barely be seen in the powder samples, being most intense in CoF_2: 3% Mn. The relative weakness of the neighbor modes may result from their being split off from the upper edge of the band and coupling poorly with $q = 0$ excitation.

The frequencies of the observed modes in $(Fe,Mn)F_2$ are shown as a function of concentration in Fig. 18. These modes are similar in most respects to those seen in $(Co,Mn)F_2$. Figure 19 shows typical spectra of this system. The AFMR of pure FeF_2 is at 53 cm^{-1}, as observed by

Ohlman and Tinkham.[2] Its behavior with added Mn is similar to that of the AFMR in (Co,Mn)F_2. The 50 cm^{-1} mode fits the description of a defect mode lying below the AFMR as predicted by Tonegawa.[55] An Ising calculation using the values in Table I gives a defect mode frequency of 48.8 cm^{-1} (neglecting nearest neighbor interactions), very close to the observed value. This lower mode differs from the corresponding 28.5 cm^{-1} mode in (Co,Mn)F_2 in that it is considerably narrower and stronger throughout the impurity concentration range. If there exists a pair mode in (Fe,Mn)F_2 which corresponds to the 32 cm^{-1} mode in (Co,Mn)F_2, it should leave an Ising frequency of about 49 cm^{-1} which is so close to the defect mode that it could not be resolved clearly. This mode and the triplet mode (Ising frequency $\approx$ 49.2 cm^{-1}) may account for the bulge on the high frequency side of the defect absorption in the 3% Mn sample in Fig. 19. There is a broad absorption between 78 and 80 cm^{-1} in the 0.1% to 3% Mn concentration range which closely corresponds to the 79 cm^{-1} Ising calculation of the neighbor mode frequency of Mn in FeF_2.

We find good qualitative agreement between the measured far-infrared modes in (Co,Mn)F_2 and the $q = 0$ mode positions calculated by Economou,[53] except at small Mn concentrations where he has neglected multiple defect modes and the splitting between the AFMR and the defect mode.

Table III lists a comparison of peak frequencies of the (Co,Mn)F_2 system at various concentrations of Mn taken from Fig. 16 compared with CPA neutron data supplied us by W. J. L. Buyers. The CPA data have been multiplied by ω to compensate for the difference between neutron and electromagnetic absorption coefficients. The resolution of the CPA calculation is only ± 1.7 cm^{-1}.

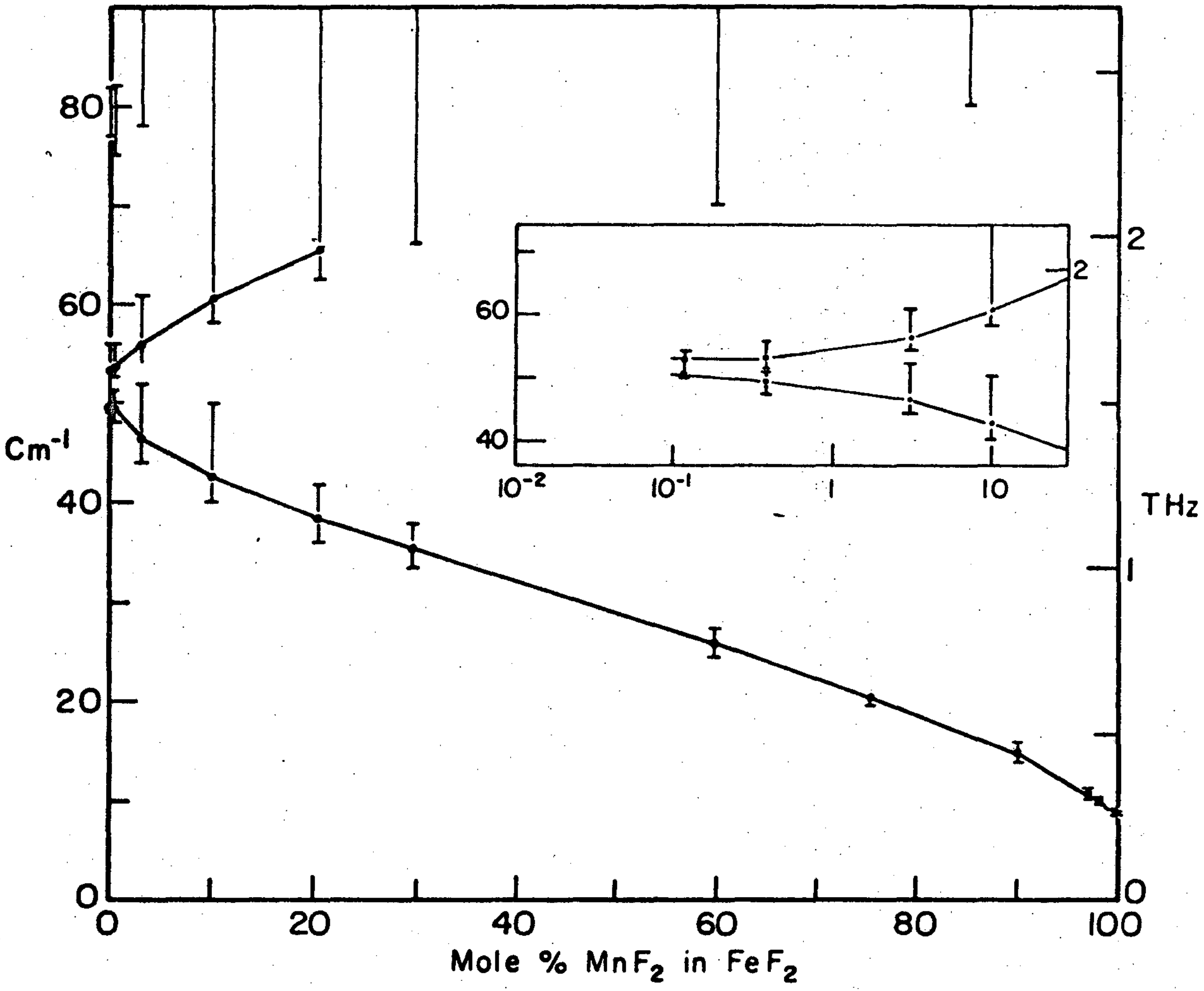

XBL 7210 - 7117A

Fig. 18. Center frequencies and widths of far-infrared absorption lines in (Fe,Mn)F_2.

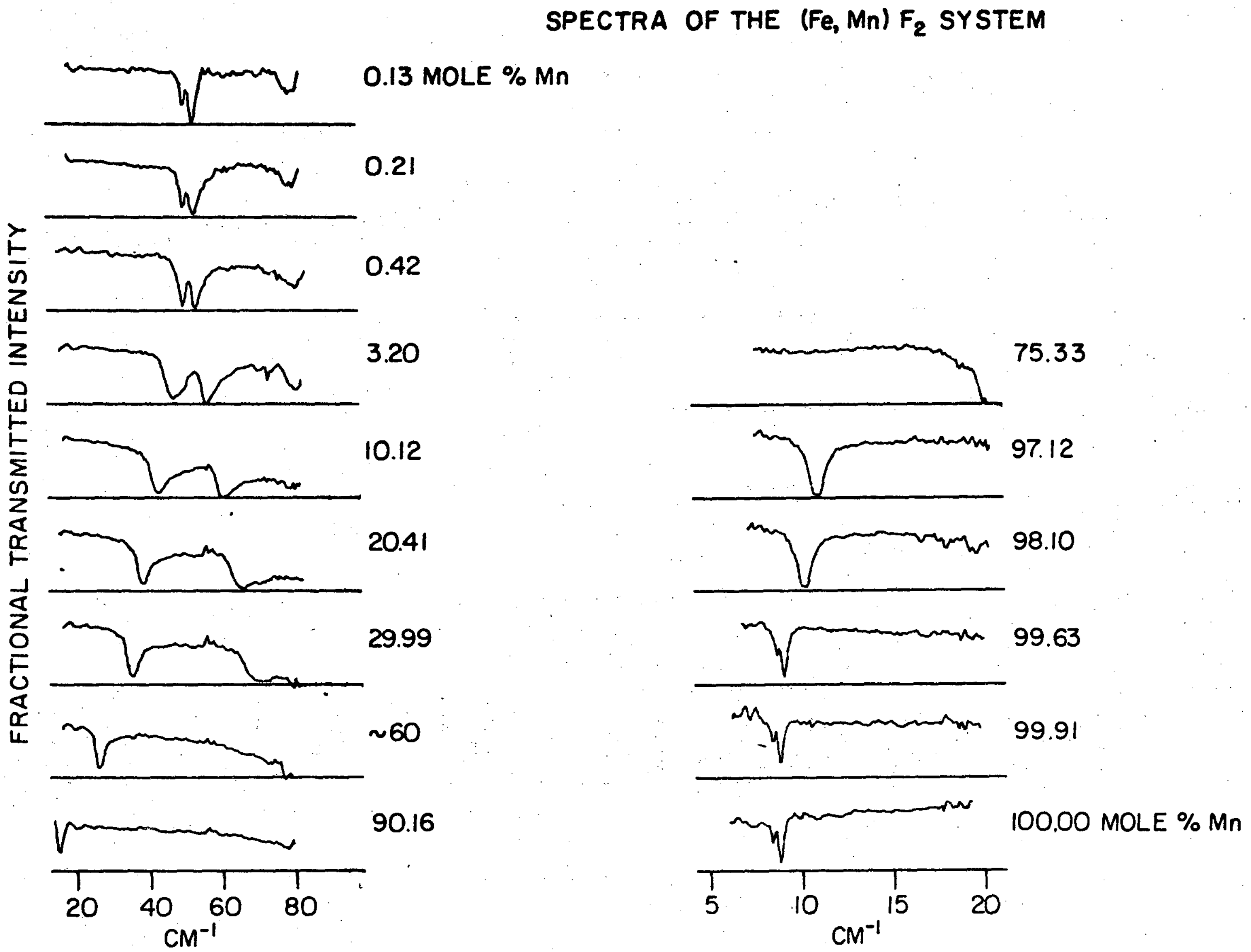

XBL 7211-7222

Fig. 19. Spectra from which some of the data in Fig. 18 were taken. SAFMR also appears in concentrated MnF_2 samples of this system.

TABLE III

Mole % Mn in CoF_2	CPA Peaks	Far-IR
3	28 cm^{-1}	27 cm^{-1}
	42 cm^{-1}	40 cm^{-1}
	68 cm^{-1}	67 cm^{-1}
5	25 cm^{-1}	26 cm^{-1}
	42 cm^{-1}	41 cm^{-1}
30	18 cm^{-1}	17 cm^{-1}
~50*	18 cm^{-1}	14 cm^{-1}
95	8.7 cm^{-1}	10 cm^{-1}

The CPA shows excellent agreement with our experimental results, the CPA values tending to be slightly high. The only datum not within the CPA resolution is a point in the heaviest alloying region.

* The far-IR sample used contained 55% Mn.

Figure 20 shows plots of CPA data compared with the measured far-IR absorption coefficient for two different Mn concentrations in the (Co,Mn)F_2 system. The agreement is seen to be quite good both in resonance position and relative strength for the lower Mn concentration. The 55% sample absorption, however, appears significantly lower in frequency and sharper than the CPA predicts.

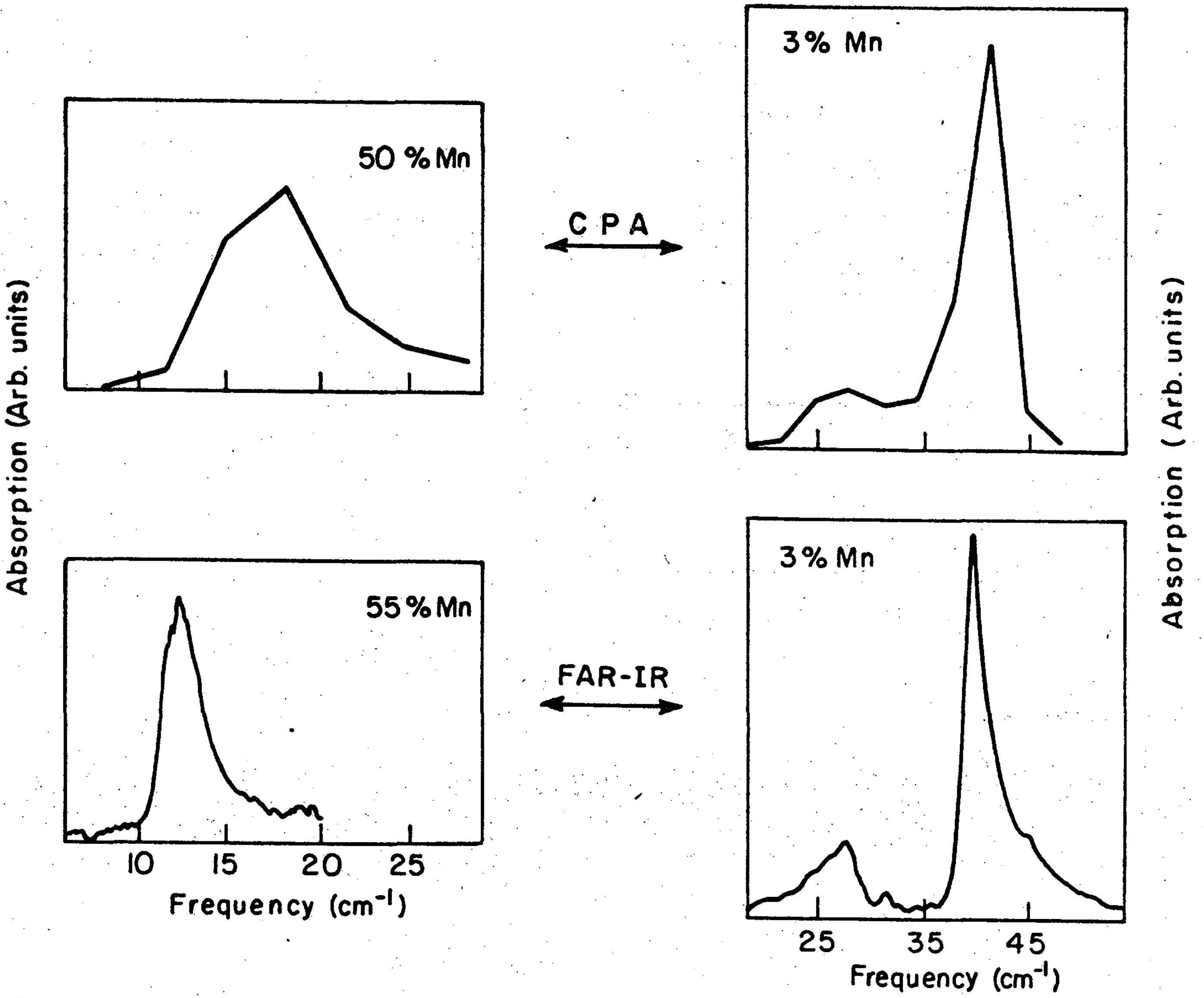

XBL741-5523

Fig. 20. Comparison of far-IR absorption coefficients with CPA neutron absorption coefficients. The neutron data have been multiplied by ω to compare to the far-IR data.

C. Results for Non-Magnetic-Magnetic System

The frequency of the AFMR of MnF_2 as a function of Zn impurity concentration is shown in Fig. 21. It is seen in these data that the AFMR decreases linearly with increasing Zn concentration to zero at ≈ 74% ZnF_2. It is interesting to compare this result with the nuclear magnetic resonance results of Baker, et al.,[56] who measured the temperature at which the F^{10} NMR lines disappeared for different Zn concentrations and found that this temperature went linearly to zero at ≈ 75% Zn concentration.

The CPA gives a reasonable fit to AFMR frequency lower Zn concentrations, but seems to be too high for very impure samples. The linewidths of both CPA and neutron results are several times larger than the far-IR linewidths. This disagreement in linewidth may be attributed to the coarse (± 1.7 cm^{-1}) resolution used in the CPA calculation.

Fig. 21. Frequency of AFMR in MnF_2 as a function of Zn concentration. Data have been ratioed to pure material frequencies for comparison. Flags indicate linewidths of our far-IR results. Of the dilute samples, the only peak shown is that of the 40% sample; all other peaks were saturated and their positions between the flags are therefore not known. The peak of the single k = 0 neutron experiment and two CPA calculated k = 0 peaks are indicated by Δ and □ respectively. The neutron and CPA data were obtained from the work of Buyers *et al.*[52]

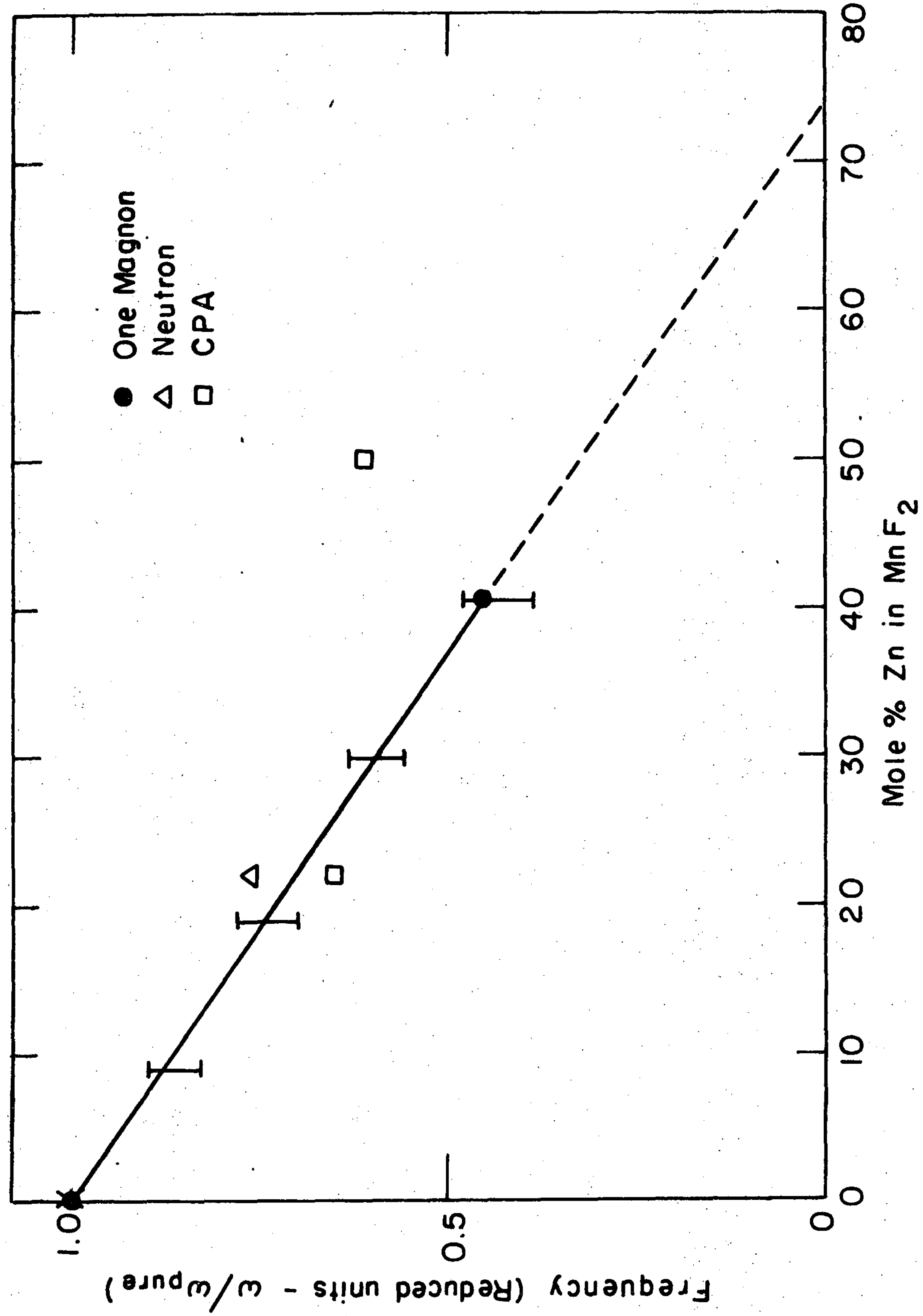

XBL 738-1625

Fig. 21

CHAPTER IV. IMPEDANCE MATCHING A SUPERCONDUCTING GALVANOMETER

A. Introduction and Experimental Detail

We have developed a superconducting transformer which performed exactly as a simple theory predicted it should and which increased the noise-limited range of a standard superconducting galvanometer (a SLUG in this case) by seven orders of magnitude. This series of experiments was carried out some time ago and some of the devices and techniques used have been superceded by higher performance methods of operation.[57] However, the main results of this work have not been reduced in importance because they concern the basic problem of impedance matching an electrical circuit to a device with zero input resistance.

The SLUG and its principles of operation have been thoroughly discussed elsewhere,[57] so we shall discuss its operation only briefly. The SLUG consists of a bead of solder frozen onto a piece of Nb wire whose insulation has been scraped away to form a bare, oxidized niobium surface. The solder makes several mechanical contacts with this surface. At low temperatures these contacts form Josephson-type weak links or junctions, and a current passed through the junctions will be a supercurrent up to some critical value, at which point a voltage develops across the junctions. Passing a second current through the niobium wire causes flux to be applied to the region between the junctions and changes the critical current. The change in critical current is periodic with a period of one quantum of applied flux. This applied flux change corresponds to a change in the niobium wire current of typically between 0.1 and a few μA.

If the solder-Nb junctions are biased at a constant current just above the critical value, the voltage across the junctions will also be periodic in the Nb wire current. With a sensitive voltmeter, changes of a very small fraction of a period may be seen. We observed these voltage changes by means of a Kiethley dc milli-microvoltmeter. Current resolution values of 5×10^{-8} A were obtained with a 0.2 sec time constant.[58]

To fit the SLUGS to our transformer design, and to reduce their inductance, we made some SLUGS in a hairpin configuration, shown in Fig. 22. The inductance of a hairpin SLUG was estimated to be about 8×10^{-8} H from a time constant measurement of the SLUG in parallel with $\approx 10^{-9}\ \Omega$ Cu resistor.

Our SLUGS were made in a bakelite jig which had an oblong, round-bottomed depression about 1 cm long, 0.5 cm wide, and 0.25 cm deep. Four terminal screws were mounted around the depression to make electrical contact with each end of a Nb wire (75 μ or 125 μ dia) and a manganin wire.[59] These wires were stretched across the depression at right angles to each other and crossed above the depression (see Fig. 23).

The Nb wire was insulated with a tough enamel of unknown composition. (Formvar did not have adequate resistance to heat.) After both wires were fastened in the jig, this insulation was scraped away with a razor blade for about 0.2 mm at some point between the manganin wire and the end of the depression. The manganin wire was tinned before being stretched across the depression. Tin-lead rosin core solder was melted into the depression until the bead surrounded both wires and covered the scraped area on the Nb wire.

At this point, if a hairpin SLUG was being made, the solder bead was allowed to freeze. The end of the Nb wire which did not have the scrape, and which had been made long for the purpose, was folded back across the

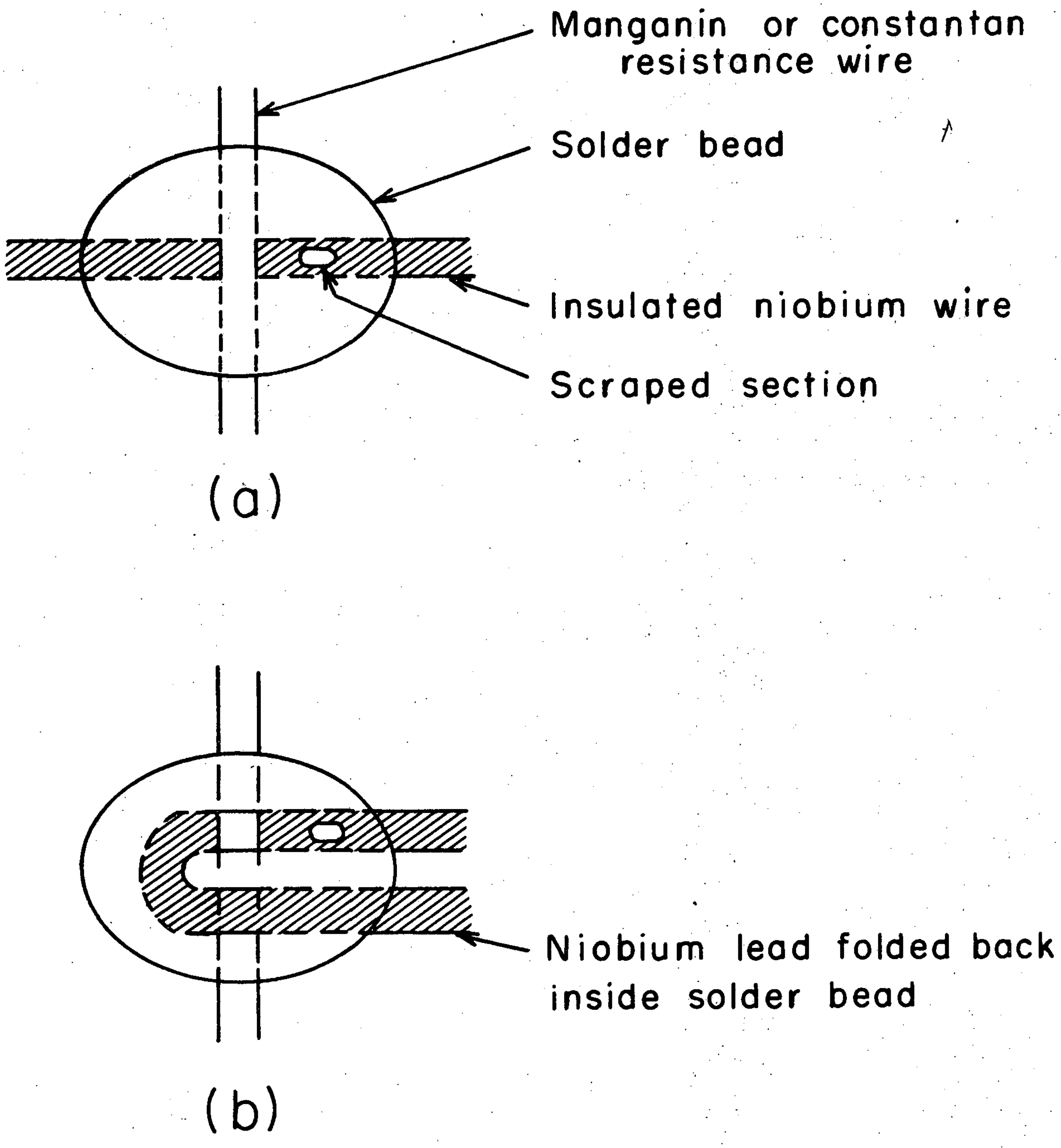

XBL7010-4049

Fig. 22. (a) Conventional SLUG, consisting of a bead of tin-lead solder on a piece of niobium wire from which the insulation has been scraped over a small section. (b) "Hairpin" SLUG in which the niobium wire is folded back on itself. This configuration has lower inductance than that of (a).

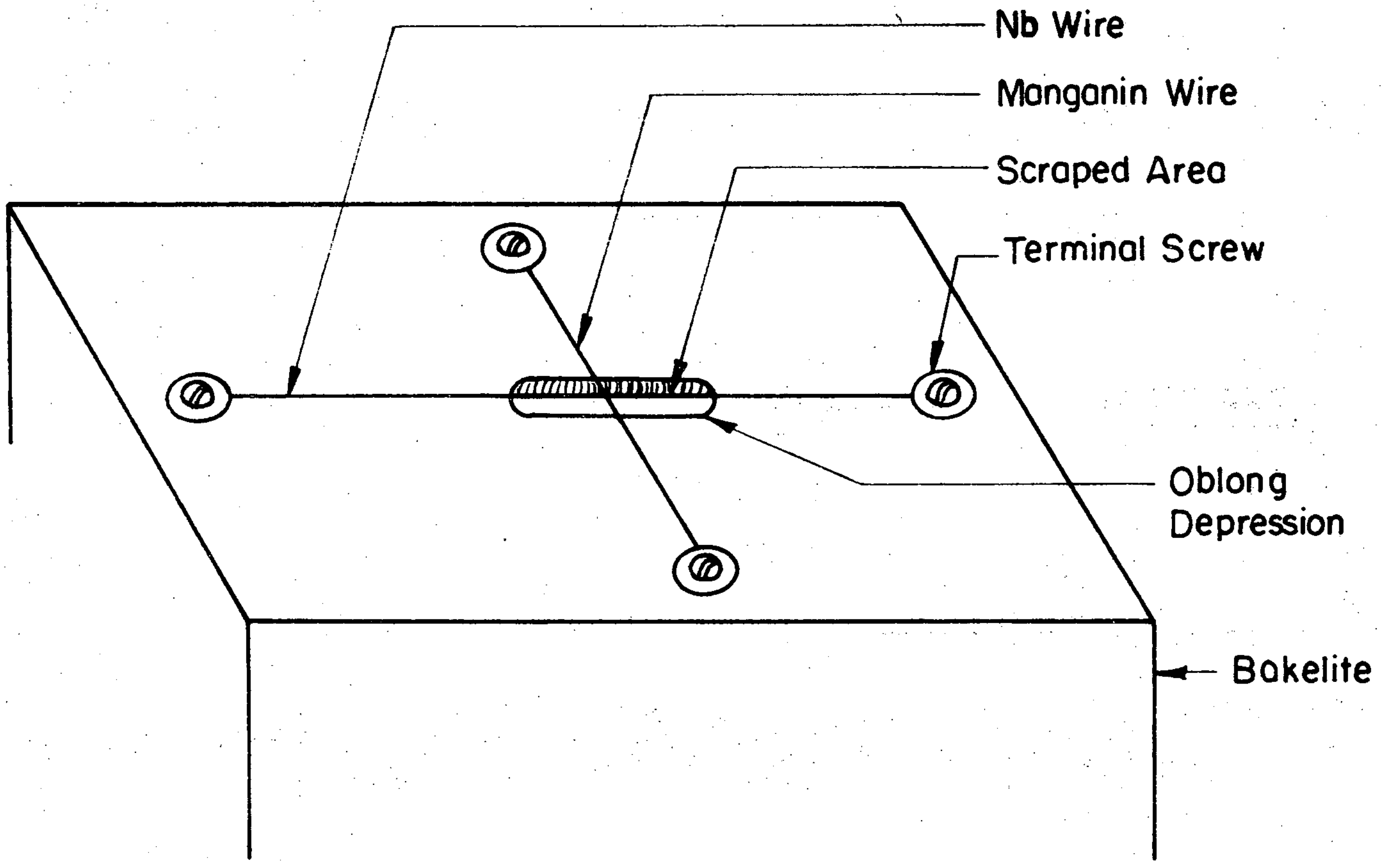

XBL7311-6631

Fig. 23. SLUG-making apparatus. Note: wires (not shown) were attached to other end of the terminal screws so that four-terminal resistance measurements of the junctions formed on the scraped section could be made.

solder bead and covered with more solder. Care was taken to insure that the Nb wire was not kinked in this folding process and thereby weakened due to work-hardening of the Nb. After folding and covering were completed, both Nb leads emerged from the same end of the bead separated by about 1 or 2 mm.

An oscillating current was applied across the junctions using one Nb lead and one manganin lead. The voltage was read across the other leads and both were displayed on an oscilloscope. The solder was partially melted near where the Nb leads emerged, and the Nb leads were gently tugged until a junction resistance of 0.4 Ω to 2.0 Ω was observed on the scope. It was important that this resistance be maintained after the solder cooled in order for the SLUG to have a good chance of working at low temperatures.

SLUGS were usually tested in batches of 9 of which typically two or three showed modulation and one or two worked well. The only two batches which did significantly better than this had 4 out of 9 and 5 out of 5 usable SLUGS, the second batch being the only batch made from a spool of 75 μ Nb wire.

B. Noise Analysis of Simple Circuits Containing Superconducting Devices

It is possible to obtain a simple criterion for comparing superconducting signal detectors with more conventional detectors by considering the NEP of the detecting circuitry. The NEP (noise equivalent power) is defined as the input signal frequency power required to produce an output signal equal in magnitude to the amplifier noise at the output. The NEP is a function of circuit design and operating conditions, and is often expressed as a function of signal frequency, source resistance, and source temperature. The simplest way of comparing two devices is to compare their NEP's under given operating conditions in a circuit appropriate to each device. We shall call a device "ideal" or "Johnson noise limited" if its amplifier NEP is less than the Johnson noise in the source resistance.

Figure 24 shows a typical voltage measuring circuit using a SLUG. The galvanometer (SLUG + room temperature amplifier) has an effective input current noise spectrum $I_G^2(f)$ which is a function of frequency. The galvanometer also has a response time τ_G. The gain of the galvanometer, G(f), would typically be a function of the form $A/1+i2\pi(f-f_o)\tau_G$. Here, A is some amplification factor and f_o is the signal frequency. R_S is the source resistance and L_S is the inductance of the detecting circuit. A practical lower limit on L_S for a SLUG is $\approx 10^{-8}$H because of the necessarily finite length of the niobium leads. $\tau = L_S/R_S$ is just the measuring circuit response time.

In this discussion, we assume that our amplifier is a dc amplifier measuring a dc signal. This is the situation corresponding to our experimental setup. However, a similar analysis could be made for finite signal frequencies, resonant circuit techniques, and lock-in detection. We shall further assume that $I_G^2(f)$ is a constant, $4I^2$, that is, we assume that the amplifier noise is white noise. Since the signal power is dissipated in the source resistance the dc NEP of the above circuit is just

$$\begin{aligned} \mathrm{NEP} &= R_S \int_o^\infty I_G^2 \frac{|G(f)|^2}{|G(0)|^2}\, df = R_S \int \frac{4I^2}{1+(2\pi f)^2 \tau_G^2}\, df \\ &= R_S \frac{I_G{}^2}{\tau_G} = \frac{L_S I^2}{\tau\tau_G} \quad . \end{aligned} \tag{41}$$

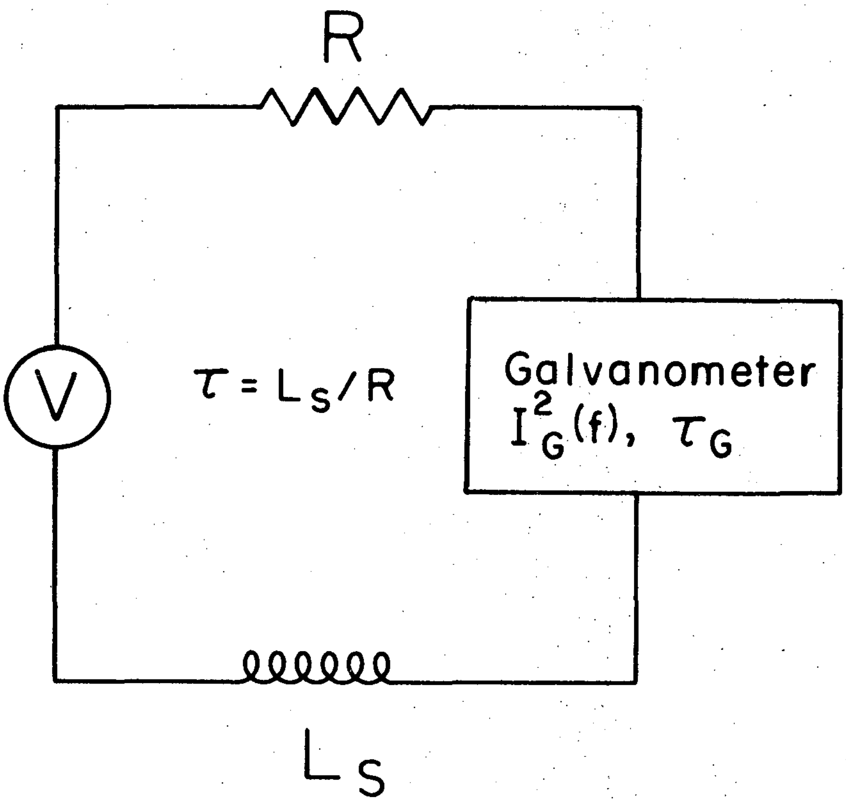

XBL7010-4023A

Fig. 24. Voltage measuring circuit for a SLUG. The SLUG and accompanying amplifying electronics are lumped together in the rectangle marked "Galvanometer". R_S is the source resistance, L_S is the inductance in the measuring circuit (taken to be as small as possible, and usually limited to $\gtrsim 10^{-8}$ H by the length of the Nb SLUG leads), $\tau = L_S/R_S$ is the measuring circuit response time, and $I_G{}^2(f)$ is the output noise power spectrum referred to the current input of the SLUG (f is frequency.)

The Johnson noise power must similarly be referred to the input:

$$N_J = 4kT \int_0^\infty \left(\frac{1}{1+(2\pi f)^2\tau^2}\right)\left(\frac{1}{1+(2\pi f)^2\tau_G^2}\right) df = \frac{kT}{\tau+\tau_G} \tag{42}$$

where T is the source temperature. In any experimental circumstance it is desirable to minimize the total noise (N_J + NEP) for a given system response time $\tau+\tau_G$. This condition requires that $\tau = \tau_G$. Under this condition we find that the SLUG is ideal when

$$\frac{R_S I^2}{\tau} \leqslant \frac{kT}{2\tau} \Rightarrow 2R_S I^2 \leqslant kT. \tag{43}$$

Figure 25 shows the "ideal" region for a SLUG.

It is an interesting consequence of our assumption of white amplifier noise that there is no temperature below which a SLUG cannot see Johnson noise in some small resistor. However, in real amplifiers the 1/f component of $I_G^2(f)$ will effectively limit τ_G to some finite value $\tau_{G(max)}$ and thereby place an effective lower bound to the temperatures for which the SLUG can be "ideal." This lower bound is called the noise temperature and is given by

$$T_G = \frac{L_S I^2}{k\tau_{G(max)}} . \tag{44}$$

Since we had no time constant adjustment on our room temperature voltmeter, we had a practical limit of $\tau_G \approx 0.2$ sec. The minimum detectable current or galvanometer sensitivity under these conditions was $I_G = \sqrt{I^2/\tau_G} = 5 \times 10^{-8}$ A as mentioned before.

Fig. 25. Ideal operating region for a SLUG. For sources with temperatures and resistances in the shaded region, the SLUG can see Johnson noise in the source resistance. The dotted vertical line represents a measuring time constant τ of 1 sec (a total time constant of 2 sec), which is arbitrarily taken to be a practical limit on signal measurements. For all sources to the left of this line, it would take longer than 1 sec to see Johnson noise.

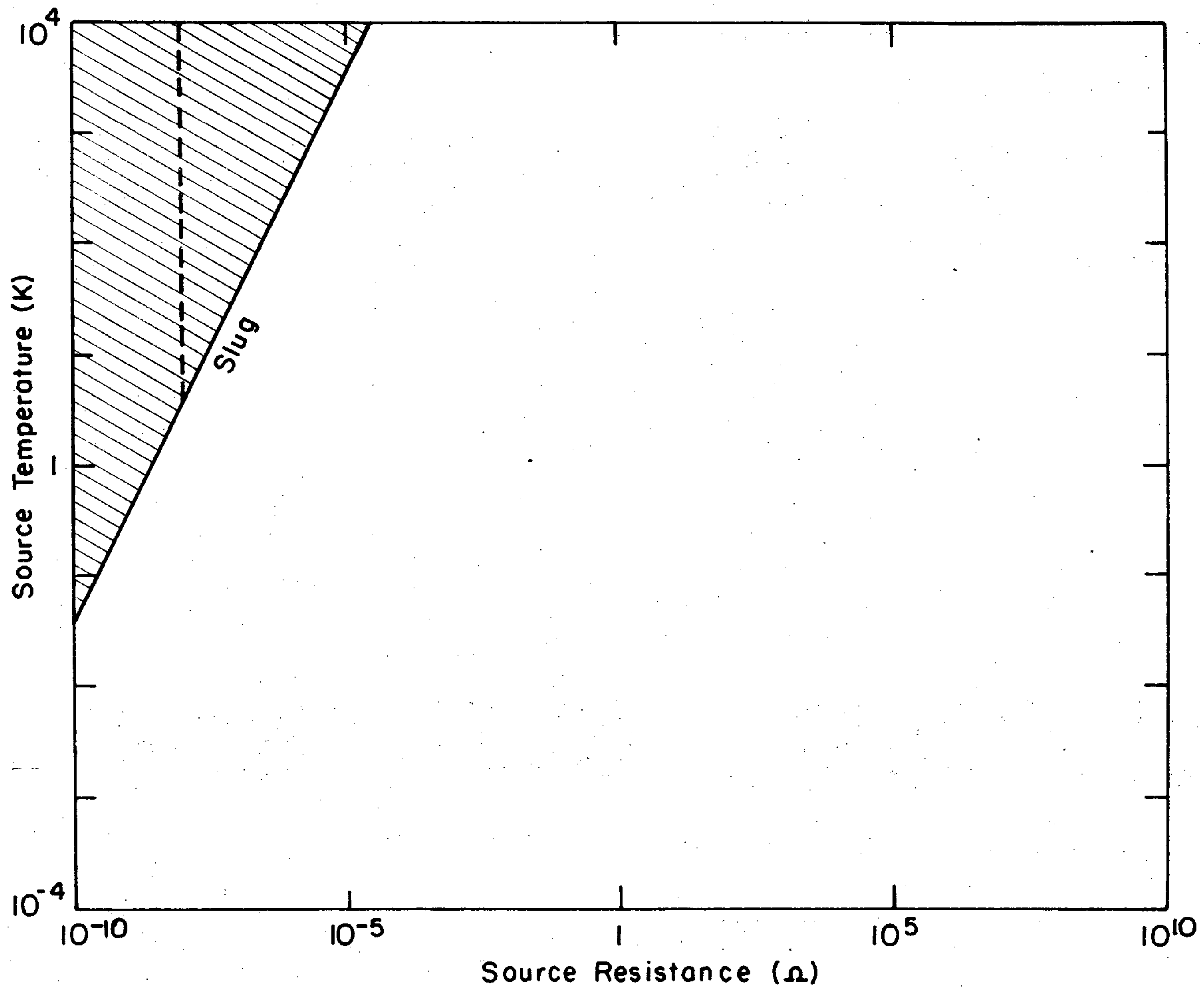

XBL738-1626

Fig. 25

For a SLUG with our instrumentation T_G was about 1.8K. The critical resistance below which the bolometer is ideal at 4.2K is about 10^{-8} Ω, as seen from Fig. 25.

There are applications in which one would like to use an ideal voltmeter with low-temperature resistances appreciably above 10^{-8} Ω, but below the values where a conventional (nonsuperconducting) voltmeter is applicable. One possible way of achieving this end is to increase the galvanometer sensitivity I_G. There are certainly Josephson devices[57] with resolutions of 10^{-8} A or better which are more sensitive than the SLUG. However, a method of improving the current sensitivity of any given superconducting galvanometer is to use an impedance-matching superconducting transformer, which may be used at zero frequency. The galvanometer is mounted in a superconducting loop so that a magnetic field applied to the loop generates a circulating current which is measured by the galvanometer. This loop forms the secondary of the transformer. If the field is generated by an ideally coupled primary coil of N turns, the current gain of the transformer will be N. In practice, the coupling will be less than perfect and the current gain less than N. A further effect of the coupling is to reduce the effective primary inductance. Elementary transformer theory shows that coupling a resistanceless secondary to a primary inductance L_p lowers the effective inductance of the primary to $L_p(1 - k^2)$, where k is the coupling constant. This decrease in inductance arises from the flux cancellation of the secondary screening currents. A coil has self-inductance because it is linked by magnetic flux proportional to the current flowing through it. A superconducting secondary loop placed in this flux generates a supercurrent which excludes flux from its interior. The field of this screening current cancels a fraction k^2 of the flux linking the primary and thereby reduces its self-inductance by an amount L_pk^2.

In the case of an ideal transformer ($k = 1$), the current sensitivity referred to the primary will be $I_p = I_G/N$ and there will be no contributions to the inductance of the primary circuit from the primary coil. If we assume the galvanometer inductance to be L_s, an inductance $L = N^2L_s$ will be reflected into the primary. However, the noise temperature $k^{-1}LI_p^2 = k^{-1}L_sI_G^2$ is the same as for the galvanometer alone. If we replace I_G by I_G/N in Eq. (5), we see that the critical resistance in the primary circuit of the transformer-galvanometer combination increases as N^2. In principle then, the resistance range of a superconducting galvanometer may be increased indefinitely by means of an ideally coupled transformer. In practice, of course, the coupling is not ideal and the range may be extended only by a finite amount. The following sections deal with the theory, design, and construction of a superconducting transformer.

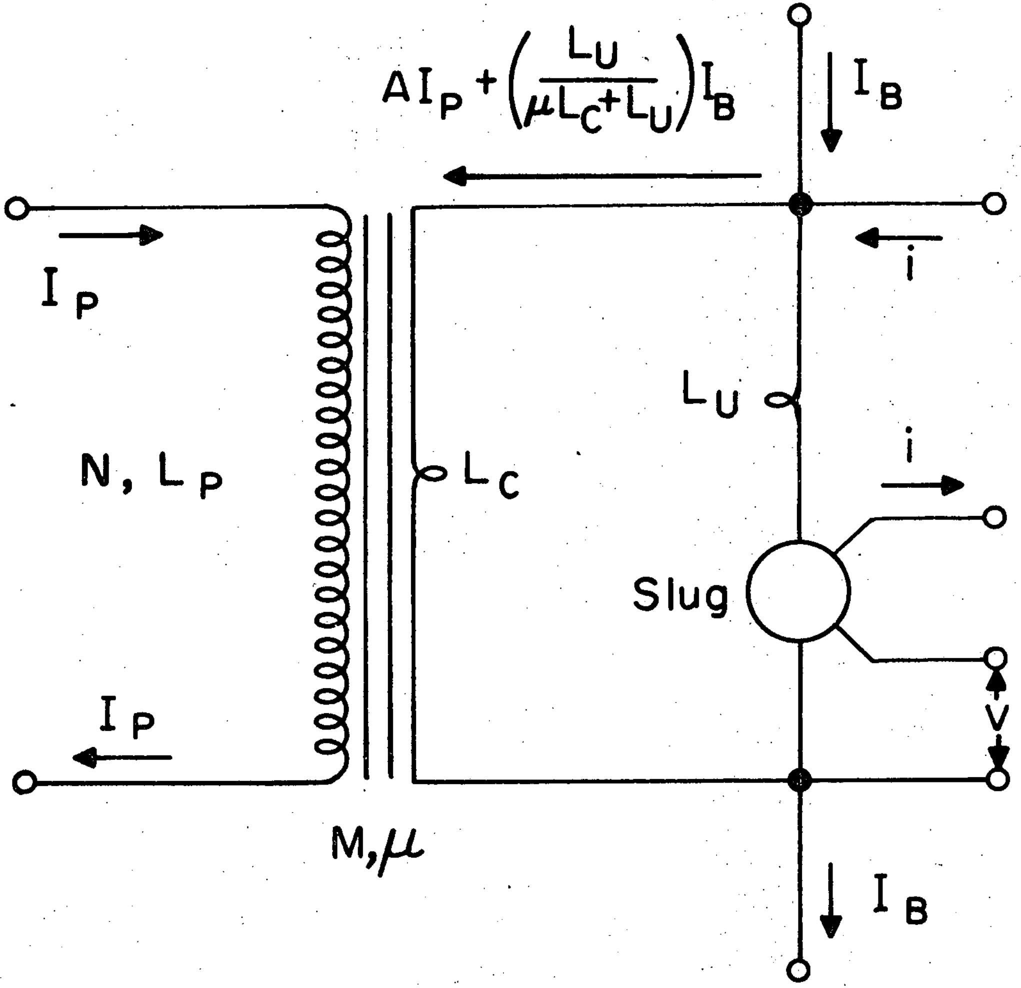

XBL7010-4022

Fig. 26. Schematic of superconducting transformer. The primary contains N turns of inductance L_p. The secondary has an inductance L_c partly coupled to the primary and an inductance L_U completely uncoupled from the primary. M is the mutual inductance between L_p and L_c and the permeability of the core. The critical current of the SLUG is measured by means of the leads (i) and (v). A current I_B biases the SLUG on the steepest part of an oscillation.

C. Theory of the Transformer

The main objective of our transformer design is to make the coupling between primary and secondary as high as possible in order to maximize the current gain and at the same time minimize the primary inductance. We now explore this problem in some detail.

In practice, the greatest problem in obtaining ideal coupling is the presence of the irregularly shaped SLUG in the secondary. We assume that the stray inductance L_U associated with the SLUG is completely uncoupled from the primary. The remaining inductance L_C in the secondary loop may be at least partially coupled to the primary. We assume that the transformer contains a μ-metal core to increase this coupling. We introduce the following parameters for the primary and secondary (see Fig. 26): $N \equiv$ number of primary turns; $I_p \equiv$ primary current; $L_p \equiv$ primary inductance; $\Phi_p \equiv L_p I_p / N$ = flux linking primary in the ideal situation where all the flux generated by I_p passes through all N turns; $I_S \equiv$ secondary current; $L_c \equiv$ portion of secondary inductance which may be partially coupled to primary; $L_U \equiv$ uncoupled portion of secondary inductance (described above); and $\phi_c \equiv L_c I_s$.

The following parameters depend on the geometry of the primary and and secondary taken together: $M \equiv$ mutual inductance of L_p and L_c; $\phi_{pc} \equiv MI_p \equiv k_{pc}\phi_p$ = portion of ϕ_p linking L_c in the absence of screening currents in the secondary ($k_{pc} \leqslant 1$); $\phi_{cp} \equiv (M/N)I_s \equiv k_{cp}\phi_c$ = portion of ϕ_c linking L_p in the absence of screening currents in the primary ($k_{cp} \leqslant 1$); $\mu \equiv$ factor by which flux linking L_c is amplified by the μ-metal core.

We note that k_{pc} and k_{cp} need not be equal if the geometries of the primary and secondary are different. For example, if a single-turn secondary of fixed radius were coaxial at the midpoint of a long solenoid of N turns and the same radius, virtually all of the flux generated by a current in the solenoid would pass through the secondary ($k_{pc} \simeq 1$). On the other hand, most of the flux generated by a current in the secondary would link only a few turns of the solenoid[60] ($k_{cp} \ll 1$). Also, note that a relationship exists between k_{pc} and k_{cp}, namely,

$$k_{pc}L_p/N = M = k_{cp}NL_c. \tag{45}$$

The basic quantities of interest in transformer design are the amplification

$$A \equiv |I_s|/|I_p| \tag{46}$$

and the effective primary inductance L_E. The effective primary inductance is proportional to the total flux ϕ_T which links the primary. There are two contributions to ϕ_T. The first is the flux ϕ_p generated by I_p and the second is the flux generated by the response of the superconducting secondary and the core. Let us consider first the situation in which $L_U = 0$. In this case, screening currents in L_c prohibit flux from linking the secondary or core. The effect of this screening is to contribute to ϕ_T an amount $-k_{cp}\phi_{pc} = -k_{cp}k_{pc}\phi_p$.

The effective inductance is therefore $L_p(1 - k_{cp}k_{pc})$. On the other hand, if L_U is non-zero, some flux is able to link L_c and the core. However, the total flux in the secondary remains zero because the flux linking L_c is exactly cancelled by that linking L_U.

The quantity of flux ϕ which now links L_c and therefore partially links the primary may be found by solving

$$\phi = \mu(\phi_{pc} + L_c I_s) \tag{47}$$

and

$$0 = L_U I_s + \phi \tag{48}$$

to obtain

$$\phi = \mu\phi_{pc}L_U/(\mu L_c + L_U). \tag{49}$$

The effective inductance L_E is given by

$$L_E = (N/I_p)[\phi_p(1 - k_{pc}k_{cp}) + k_{cp}\phi]$$

$$= L_p[(1 - k_{pc}k_{cp}) + k_{pc}k_{cp}\mu L_U/(\mu L_c + L_U)]. \tag{50}$$

We determine the amplification A from Eqs. (45)-(48):

$$A \equiv \left|\frac{I_s}{I_p}\right| = \frac{\mu k_{pc} L_p}{N(\mu L_c + L_U)} = \frac{\mu L_c k_{cp} N}{\mu L_c + L_U} . \qquad (51)$$

L_E may be written in terms of the independent paramters A, L_c, L_U, μ, k_{cp}, and k_{pc} in the form

$$L_E = L_c A^2 \left(1+ \frac{L_U}{\mu L_c}\right)^2 \left(\frac{1}{k_{cp} k_{pc}}\right) + A^2 L_U \left(1+ \frac{L_U}{\mu L_c}\right) . \qquad (52)$$

Equation (52) expresses the result that for a given value of A, the lowest value of L_E is achieved by making L_U as small as possible and the coupling coefficients as near to unity as possible.

In the limit $L_U \ll \mu L_c$, the current amplification becomes

$$A = N k_{cp} . \qquad (53)$$

In this limit, the effective inductance may be written from Eqs. (45), (50), and (53)

$$L_E = L_p(1 - k_{pc} k_{cp}) + A^2 L_U . \qquad (54)$$

If $L_c \gg L_U$, this result follows even for $\mu = 1$ and there is little to be gained by using a high-permeability core. However, if L_c and L_U are comparable, there is a distinct advantage to using a core.

We may summarize our conclusions by saying that for a given value of gain, the transformer should be designed to have the lowest value of primary inductance L_p, the lowest value of stray inductance L_U from the galvanometer, and the best possible coupling between primary and secondary. If the inductances L_U and L_c are comparable, there is a considerable advantage to using a high-permeability core; if $L_c \gg L_U$, there is little advantage.

D. Practical Transformers

1. Transformer Design and Construction

Our basic design philosophy was to wind the primary as a long single-layer solenoid which, for given radius and number of turns, has a much lower inductance L_p than a short multilayer coil. In order to achieve good coupling to the primary, the secondary must be correspondingly long. A typical transformer design is illustrated in Fig. 27. The primary coil was typically several hundred turns of 0.005 cm-diameter insulated niobium wire. It was wound on a Teflon rod 1 cm diameter and 11 cm long, protected with a layer of varnish, and covered with a layer of masking tape. The secondary consisted of a rectangular sheet of lead of 0.016 cm thickness wrapped around the primary with about 1 cm overlap. A strip of masking tape between the overlapping edges of the lead cylinder prevented their shorting together. Two tabs 6 mm wide were raised from the lead sheet, separated from each other by a thin layer of tape. The two niobium leads of a hairpin SLUG were soldered one to each tab with a low-melting-point solder which made mechanical joints to the niobium rather than alloying with it. Thus the solder and niobium were separated by a superconducting weak link. In practice, these joints were capable of carrying supercurrents of at least several tens of mA. The niobium wires of the SLUG

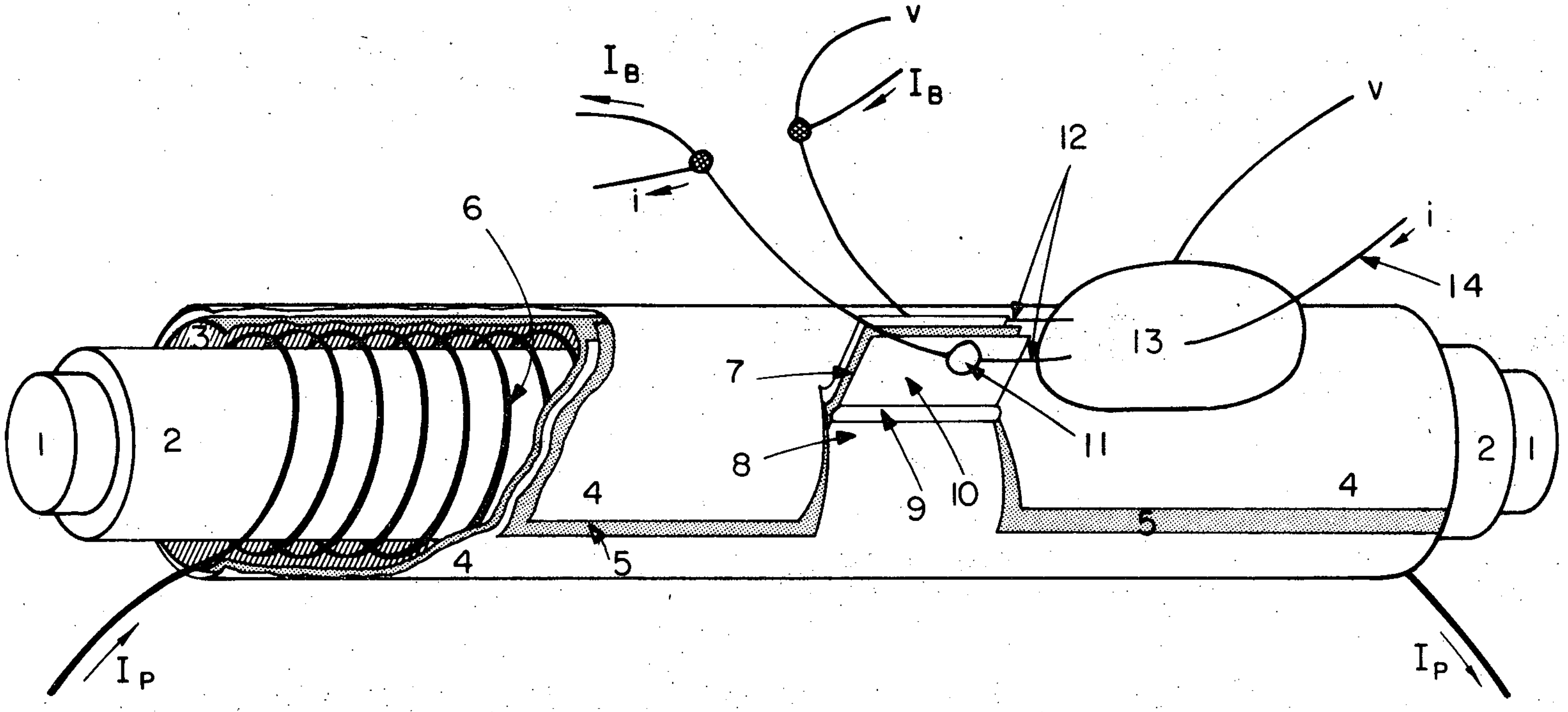

XBL7010-4021

Fig. 27. Sketch of practical superconducting transformer and SLUG. 1 is the μ-metal core, 2 is the Teflon former, 3 is the masking tape insulation between primary and secondary, 4 is the lead tape secondary, 5 is the masking tape insulation between overlapped portions of secondary, 6 is the primary windings, 7 is the masking tape insulation between tabs, 8 is the lead tab cutout of secondary, 9 is the solder joining lead and indium tabs, 10 is the indium tab, 11 is the solder joining SLUG lead to tab, 12 is the superconducting SLUG leads (niobium), 13 is the SLUG galvanometer, and 14 is the constantan leads to SLUG.

were made as short as possible to minimize the stray inductance L_U. The uncovered length of the niobium wires between the tabs and the SLUG was 1-2 mm and their separation on the same order.

In a slightly different design, the primary was wound over the secondary. The performance of the two types was similar. In a further configuration, the primary was wound as a multilayer coil about 4 mm long. Lastly, a transformer was constructed in which the edges of the lead cylinder were not overlapped but separated by a gap of about 1 mm.

A permeable core consisting of 0.1-mm μ-metal rolled into a rod could be inserted into a 7.5-mm diameter hole in the Teflon former. The effective permeability of this core, that is, the factor by which the inductance of the primary (in the absence of the secondary) was increased, was about 15.

2. Measurement of Transformer Characteristics

The two important parameters of the transformer are its current gain and the effective inductance of the primary.

In principle, the measurement of the current gain is straightforward. A small current I_p is introduced into the primary and a corresponding current I_s fed into the niobium wire of the SLUG so as to exactly cancel the the effect of I_p. The ratio I_s/I_p represents the amplification. In practice, the current I_s must be introduced at the tabs of the secondary so that the applied current divides, a fraction $\mu L_c/(\mu L_c + L_U)$ actually flowing through the SLUG. The measured current amplification is therefore higher than the true amplification. This difficulty was overcome by replacing the lead tabs on the lead cylinder with indium tabs.[61] The true period of the SLUG was determined with the tabs in the normal state.

The temperature was lowered so that the tabs became superconducting and the apparent period determined. This technique enabled the true gain of the transformer to be determined. In addition, the uncoupled inductance L_U could be estimated from the relation

$$P_N/P_S = (1 + L_U/\mu L_c)^{-1}, \tag{55}$$

where P_N and P_S are the measured periods of the SLUG with the indium tabs in the normal and superconducting states, respectively.

The effective inductance of the primary was measured by connecting it in parallel with a known resistance R, chosen so that the primary time constant $\tau = L_E/R$ was several sec. A current was switched into the resistance. As this current flowed into the primary, the critical current of the SLUG oscillated with a frequency which decayed exponentially with time. This exponential decay enabled us to estimate τ and hence L_E.

Finally, we measured $k_{pc}k_{cp}$ by winding a 500-turn superconducting coil on a hollow lead cylinder whose overlapping edges were soldered together. From the measured effective inductance of the primary, we deduced a value for $k_{pc}k_{cp}$ of 0.94.

3. Performance of Transformers

The specification and performance of four transformers are summarized in Table IV. The values of the primary inductance L_p were calculated rather than measured. The noise temperature for the transformer-SLUG combination is $k^{-1}L_E(I_G/A)^2$, where L_E is the effective primary inductance and I_G/A is the current resolution in the primary circuit.

It is clear that transformer 1 had the highest performance. Removal

TABLE IV. Specification and performance of superconducting transformers. The values of the noise temperature $T_G = k^{-1}L_E(I_G/A)^2$ are based on a value of $I_G = 5 \times 10^{-8}$ A:

	Type	Number of turns	Gain (A)	L_E (mH)	L_p (mH)	T_G (K)
1.	Monolayer primary, about 10 cm long, and 1 cm diameter, secondary on top of primary. Core with effective $\mu \approx 15$.	1000	565	4	0.8	2.3
2.	As 1, but with no core.	1000	100	0.5	0.8	9.1
3.	Monolayer primary, about 5 cm long, 1.4 cm diameter, primary on top of secondary. Edges of lead cylinder not overlapped. No core.	500	55	0.6	0.6	36
4.	Short multilayer coil, about 4 mm long, wound on top of secondary on 2-cm diameter former. No core.	1000	385	11	30	13.4

of the μ-metal core, as in transformer 2, multiplied the noise temperature by about 4. Failure to overlap the edges of the lead cylinder, as in transformer 3, increased the noise temperature by a further factor of 4. Transformer 4, with a short multilayer primary and no core, had a noise temperature about 50% higher than transformer 2.

It is apparent that only transformer 1 had an ideal performance in the He^4 range. However, it is important to realize that the use of a more sensitive Josephson device would improve the noise temperatures appreciably. For example, if we substituted a SLUG with a current resolution of 10^{-8} A, the noise temperatures would be reduced by a factor of 25 and they would all be comfortably in the He^4 range.

4. Discussion

We now examine the parameters of transformer 1 in relation to the theory developed earlier. We first estimate the stray inductance L_U associated with the SLUG and its wiring to the transformer. We assume the following values for the various parameters: $N = 1000$, $L_c = 8 \times 10^{-10}$ H (calculated), $\mu = 15$ (measured), $L_p = 0.8$ mH (calculated), $L_E = 4$ mH (measured), $k_{pc}k_{cp} = 0.94$ (measured), and $A = 565$ (measured). We further assume $k_{pc} = k_{cp}$. From Eq. (51), we find $L_U \simeq 8$ nH; from Eq. (52), 8 nH; and from Eq. (55), 9 nH. These values are consistent with each other and with the inductance of a SLUG and its wiring measured independently. We conclude that there is little flux leakage from the split cylinder forming the secondary. Flux leakage along the slit would have lowered the values of k_{pc} and k_{cp} and led to a high apparent value of L_U as estimated using $k_{pc}k_{cp} = 0.94$.

It appears that $\mu L_c \simeq 1.5\ L_U$ for transformer 1. Consequently, a core of higher permeability could have been used with advantage. Equation (54) is not a very good approximation for the effective primary inductance. With a higher permeability core, the second term on the right-hand side of Eq. (54) would have dominated the first and the equation reduced to $L_E \simeq A^2 L_U$. Under these circumstances, the noise temperature of the transformer-SLUG combination would have been the same as that of the SLUG along; in fact it was about 25% higher.

The effect of the transformer on the ideality of the SLUG is easily seen by modifying Eq. (53) to include the transformer

$$2\ R_c \frac{I^2}{N^2} \leqslant kT. \tag{56}$$

Figure 28 shows the increased ideal range of our practical transformer device. The device is compared with a top-of-the-line FET preamp.

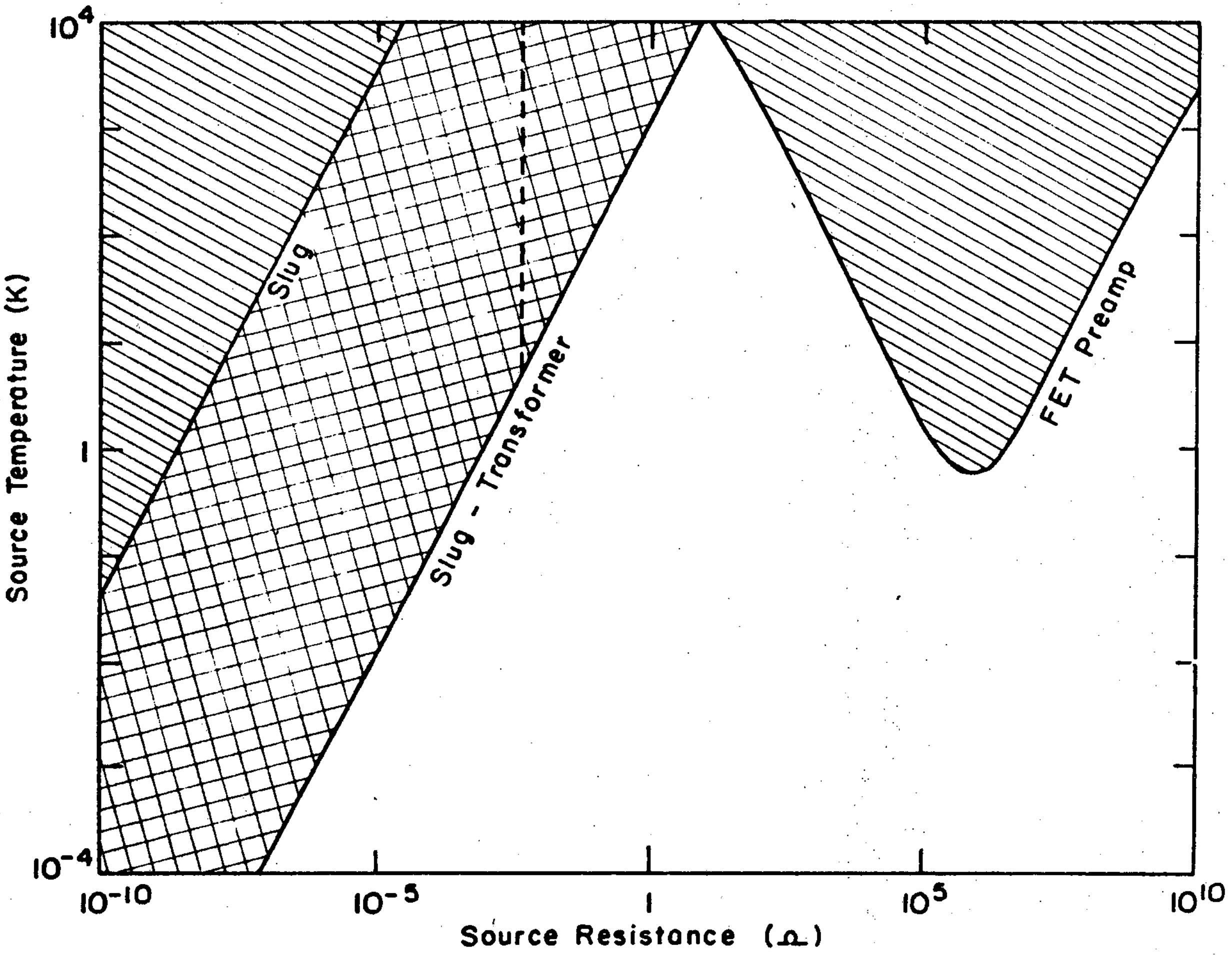

XBL738-1627

Fig. 28. Increase in ideal range of SLUG due to practical superconducting transformer (indicated by cross hatching). The parabolic shaded region is the ideal region for a Princeton Applied Research Corp. Model 185 FET preamp operating at its optimal frequency.

ACKNOWLEDGEMENTS

"It is the glory of God to conceal things,
But the glory of kings is to search things out."
—— Proverbs 25:2 (RSV)

I would like to thank my advisor, Professor Paul L. Richards, not only for his wise guidance, supervision, and advice, but also for the example he set for me as a physicist. Professor John Clarke has been a great help to me in my first attempts at experimental physics and with numerous subsequent counsels. Mr. Richard Aurbach, Mr. Robert Bailey, Mr. John Mather, Mr. David Woody, and Professor Alan M. Portis have all contributed to the ideas and experimental approaches that have gone into this work. Mr. Bailey helped proof this manuscript as well. Dr. Thomas Wolfram suggested the surface magnon identification of the extra MnF_2 resonances and provided much theoretical backing. Dr. W. J. L. Buyers provided theoretical support for the alloy work. I very much appreciate the excellent art work of Ms. Gloria Pelatowski who drew the figures contained herein.

Ms. Kathy Williams deserves a double portion of thanks both for typing and mothering this manuscript, and for providing the graceful and congenial atmosphere without which thesis research loses its "pizzazz."

I would like to thank my wife, Margaret, for restoring my objectivity about myself and my work at times when I got confused about these things.

Finally, I would like to thank God for teaching me through this enjoyable research experience, and for sustaining me with practical help when I needed it.

APPENDIX

Two experiments have been carried out since this work was completed which have important bearing on the identification of the 8.3 cm^{-1} mode as a surface magnon. Both experiments have been done by Bob Bailey using the equipment described in Chapter I. The first experiment was the measurement of the spectrum of a very fine grind powder with mean particle diameter of $\approx 1\mu$ and SVR about twenty times greater than the finest grind herein reported. The results showed that the zero field mode strengths fits a dependence of $(SVR)^{0.22}$ rather than $(SVR)^{0.5}$ as expected for a surface mode. Even more important, the absorption coefficient plot of the field on/field off ratios show that the unsaturated mode intensity is essentially the same as that given in the finest grind powder reported above. Thus the mode strength appears to have increased little if at all in the extra fine grind.

The second experiment is a microwave run taken on a $\approx$ 5 mil (011) surface single crystal. In some runs two modes were seen in close to the same position as those seen on the 111 face. In these runs the AFMR was seen. The 011 modes were broader and not as deep as the 111 mode. Subsequently, these modes were seen in some runs made with no MnF_2 sample in the waveguide. It is assumed therefore that these two resonances are due to paramagnetic contaminants which were inadvertantly admitted into the waveguide.

REFERENCES

1. F. M. Johnson and A. H. Nethercott, Jr., Phys. Rev. 114, 705 (1959).
2. R. C. Ohlman and M. Tinkham, Phys. Rev. 123, 425 (1961).
3. P. L. Richards, J. Appl. Phys. 34, 1237 (1963).
4. P. L. Richards, J. Appl. Phys. 35, 850 (1964).
5. A. Okazaki, K. C. Turberfield, and R. W. H. Stevenson, Phys. Letters 8, 9 (1964).
6. O. Nikotin, P. A. Lindgard, and O. W. Dietrich, J. Phys. C 2, 1168 (1969).
7. Kevin C. O'Brien, J. Appl. Phys. 41, 3713 (1970).
8. M. F. Thorpe, J. Appl. Phys. 41, 892 (1970).
9. J. P. Kotthaus and V. Jaccarino, Phys. Rev. Letters 28, 1649 (1972).
10. J. P. Kotthaus and V. Jaccarino, Magnetism and Magnetic Materials 1972, C. D. Graham, Jr. and J. J. Rhyne, eds. (AIP, N.Y., 1972).
11. A. S. Barker, Jr. and J. A. Ditzenberger, Solid State Communications 3, 131 (1965).
12. H. Brunner and K. F. Renk, J. Appl. Phys. 41, 2250 (1970).
13. S. J. Allen, Jr. and H. J. Guggenheim, Phys. Rev. B4, 937-68 (1971)..
14. M. T. Hutchings, B. D. Rainford, and H. J. Guggenheim, J. Phys. C3, 307 (1970).
15. A. Oseroff and P. S. Pershan, Phys. Rev. Letters 21, 1593 (1968).
16. R. Weber, Phys. Rev. Letters 21, 1260 (1968).
17. K. Johnson and R. Weber, Journal de Physique 32, C1-1070 (1971).
18. R. Weber, J. Appl. Phys. 40, 995 (1969).
19. G. Parisot, S. J. Allen, R. E. Dietz, H. J. Guggenheim, R. Moyal, P. Moch, and C. Dugautier, J. Appl. Phys. 41, 890 (1970).

20. M. Buchannan, W. J. L. Buyers, R. J. Elliott, R. T. Harley, W. Hayes, A. M. Perry, and I. D. Saville, J. Phys. C5, 2011 (1972).

21. E. C. Svensson, W. J. L. Buyers, T. M. Holden, R. A. Cowley, and R. W. H. Stevenson, Magnetism and Magnetic Materials 1971, C. D. Graham, Jr., and J. J. Rhyne, eds. (AIP, N.Y., 1971), p. 1315.

22. R. A. Cowley and W. J. L. Buyers, Rev. Mod. Phys. 44, 406 (1972).

23. For a discussion of the superexchange interaction and other properties of antiferromagnets see Ryogo Kubo and Takeo Nagamiya, Solid State Physics (McGraw-Hill, N.Y., 1969) chs. 8, 10; and articles by Simon Foner and P. W. Anderson in Magnetism I, George T. Rado and Harry Suhl, eds. (Academic Press, N.Y., 1963).

24. Simon Foner, "Antiferromagnetic and Ferrimagnetic Resonance," article in Magnetism I, see reference 23.

25. Simon Foner, (private communication).

26. P. L. Richards (private communication).

27. Observation of nominally pure samples on band-description does not agree with 14th Ed of Handbook of Chemistry and Physics.

28. Handbook of Chemistry and Physics, 47 ed., Robert C. Weast, ed. (Chemical Rubber Co., Cleveland, 1966).

29. Frederic Keffer, Phys. Rev. 87, 608 (1952).

30. Measured orientation of cleavage faces by X-ray and measured dihedral angle between cleavage plane and other crystal faces which had been cut in known orientation. These faces are the planes of highest atomic density.

31. CoF_2 effective spin depends on magnetic surroundings because of mixing of higher states. Also the exchange integrals for CoF_2 are

anisotropic. See Ref. 22.

32. R. Loudon and P. Pincus, Phys. Rev. 132, 673 (1963).

33. See, for example, K. D. Möller and W. G. Rothschild, Far-Infrared Spectroscopy, (John Wiley & Sons, Inc., N.Y., 1971).

34. R. R. Joyce and P. L. Richards, Phys. Rev. 179, 375 (1969).

35. Frank J. Low, J. Opt. Soc. Am. 51, 1300 (1961).

36. R. Clark Jones, J. Opt. Soc. Am. 43, 1 (1953).

37. R. R. Joyce, Ph.D. Thesis, University of California, Berkeley, 1970.

38. P. L. Richards, "Fourier Transform Spectroscopy", in Spectroscopic Techniques for Far Infra-Red Submillimetre and Millimetre Waves, D. H. Martin, ed. (North-Holland Publishing Company, Amsterdam, 1967) p. 33.

39. D. L. Mills and W. M. Saslow, Phys. Rev. 171, 488 (1968).

40. T. Wolfram and R. E. DeWames, Phys. Rev. 185, 762 (1969).

41. T. Wolfram, R. E. DeWames, and E. A. Kraut, J. Vac. Sci. & Technol. 9, 685 (1972) and references therein.

42. R. H. Ritchie, Phys. Rev. 106, 874 (1957) and E. A. Stern and R. A. Ferrell, Phys. Rev. 120, 130 (1960).

43. T. Wolfram, private communication.

44. G. A. Somorjai, private communication.

45. L. Genzel and T. P. Martin, Surface Science 34, 33 (1973).

46. A. James Henderson, Jr., David G. Onn, Horst Meyer, and J. P. Remeika, Phys. Rev. 185, 1218 (1969).

47. A. M. Portis and A. C. Gossard, J. Appl. Phys. 31, 250 S (1960).

48. W. Wolf, private communication.

49. T. Holden, private communication.

50. D. Woody, private communication.

51. W. J. L. Buyers, D. E. Pepper, and R. J. Elliott, J. Phys. C5, 2611 (1972).

52. W. J. L. Buyers, D. E. Pepper, and R. J. Elliott, J. Phys. C6, 1933 (1973).

53. E. N. Economou, Phys. Rev. Letters 28, 1206 (1972).

54. S. K. Lyo, Phys. Rev. Letters 28, 1192 (1972).

55. T. Tonegawa, Prog. Theor. Phys. 40, 1195 (1968).

56. J. M. Baker, J. A. J. Lourens, and R. W. H. Stevenson, Proc. Phys. Soc. 77, 1038 (1961).

57. For a good review, see J. Clarke, IEEE Proceedings 61, 8 (1973) and references therein.

58. Best SLUGs we have made could resolve better than 10^{-8} A. We have taken 5 × 10^{-8} A as a more typical figure.

59. We usually used resistance wire (manganin or constantan) rather than copper wire to make connections to the solder bead. The resistance wire has a much lower thermal conductance than copper and minimizes the heating of the SLUG when it is soldered into a circuit.

60. It is also interesting to note that for a primary and a secondary to be perfectly coupled ($k_{pc} = k_{cp} = 1$, $L_U = 0$), in the absence of screening currents all flux which links one circuit must link the other. Therefore the geometries of the primary and secondary must be exactly superposed--the path taken by the secondary current must be identical to that taken by the primary current. In the case where the paths are not identical (all real situations), there are always fine flux lines linking one circuit which do not link the other.

61. 1% Bi was added to the In to increase the normal-state resistance of the tabs. The time constant of the secondary circuit was then conveniently short.

TECHNICAL INFORMATION DIVISION
LAWRENCE BERKELEY LABORATORY
UNIVERSITY OF CALIFORNIA
BERKELEY, CALIFORNIA 94720